Large Eddy Simulations of sediment entrainment induced by a lock-exchange gravity current

Foteini Kyrousi[a,b,*], A. Leonardi[a], F. Roman[d], V. Armenio[b], F. Zanello[a], J. Zordan[c], C. Juez[c], L. Falcomer[a]

[a] Idrostudi srl, Loc. Padriciano 99 Trieste, 34149, Italy
[b] Department of Engineering and Architecture, University of Trieste, Piazzale Europa 1, 34127, Italy
[c] Laboratoire de Constructions Hydrauliques (LCH), Ecole Polytechnique Federale de Lausanne (EPFL), Lausanne 1015, Switzerland
[d] Iefluids srl, Trieste, Italy

ARTICLE INFO

Accepted 1 February 2018

Keywords:
Large eddy simulation
Gravity currents
Suspended sediment transport

ABSTRACT

Large Eddy simulations of lock-exchange gravity currents propagating over a mobile reach are presented. The numerical setting allows to investigate the sediment pick up induced by the currents and to study the underlying mechanisms leading to sediment entrainment for different Grashof numbers and grain sizes. First, the velocity field and the bed shear-stress distribution are investigated, along with turbulent structures formed in the flow, before the current reaches the mobile bed. Then, during the propagation of the current above the erodible section of the bed the contour plots of the entrained material are presented as well as the time evolution of the areas covered by the current and by the sediment at this section. The numerical outcomes are compared with experimental data showing a very good agreement. Overall, the study confirms that sediment pick up is prevalent at the head of the current where the strongest turbulence occurs. Further, above the mobile reach of the bed, settling process seems to be of minor importance, with the entrained material being advected downstream by the current. Additionally, the study shows that, although shear stress is the main mechanism that sets particles in motion, turbulent bursts as well as vertical velocity fluctuations are also necessary to counteract the falling velocity of the particles and maintain them into suspension. Finally, the analysis of the stability conditions of the current shows that, from one side, sediment concentration gives a negligible contribution to the stability of the front of the current and from the other side, the stability conditions provided by the current do not allow sediments to move into the ambient fluid.

1. Introduction

Gravity currents represent an ubiquitous phenomenon in the environment and in engineering applications. They constitute essentially horizontal flows driven by the density difference with respect to the ambient fluid, and are able to travel over long distances, up to hundreds of kilometers in lakes, seas and oceans. Density gradients are caused by salinity and temperature inhomogeneities or, in case of turbidity currents, by the presence of material in suspension. They can be found under a large variety of circumstances in nature and can be caused by natural events, e.g. sea breeze storms, oceanic overflows, avalanches or airbone snow and volcanic eruption; or by anthropogenic activities, e.g., release of water with high salinity from desalination plants, accidental release of a dense gas, oil spillages or pollutant discharge in water bodies (Simpson, 1997). Another important example of gravity currents is the intrusion of salt water into a mass of fresh water (Benjamin, 1967). Such flows have the ability to erode and transport sediment, as well as oxygen and pollutants. Their propagation is frequently associated to rapid morphological changes in river and estuarine beds (Parker et al., 1987), reservoir sedimentation (Schleiss et al., 2016), damage to submarine emissaries and cables (Fine et al., 2005), and pollutant dispersion. For these reasons, the ability to predict their evolution and their capacity to entrain and deposit sediment is of great interest.

The dynamics of gravity currents have been extensively investigated in the laboratory (e.g. Garcia and Parker, 1993; Hallworth et al., 1996; Kneller et al., 1997; Lombardi et al., 2017; Nogueira et al., 2014; Nogueira et al., 2013; Ottolenghi et al., 2017a; Rottman and Simpson, 1983; Simpson, 1982), and by high-resolution numerical simulations (e.g. Gonzalez-Juez et al., 2010; Härtel et al.,

* Corresponding author.
E-mail address: kyrousi@idrostudi.it (F. Kyrousi).

2000b; Necker et al., 2005; Ooi et al., 2009; Ottolenghi et al., 2016a; Ottolenghi et al., 2017b), where the lock-exchange configuration is the dominant set-up. In this geometry, the flume is divided into two volumes by a sliding vertical gate. One volume contains the denser fluid and the other one the lighter fluid. Both fluids are initially at rest. When the gate is removed, differences in hydrostatic pressure produce a dense current which moves along the lower boundary, while a neutrally buoyant current travels in the opposite direction along the upper boundary. As a consequence, a shear layer forms between the two fluids giving use to mixing due to Kevin–Hemholtz instabilities (Simpson, 1972). Furthermore, in case of a high volume of the dense intrusion, compared to the reception volume, an important return flow may occur after the passage of the gravity current (Theiler and Franca, 2016).

The propagation of gravity currents over loose beds can trigger the entrainment of large quantities of sediment and carry or deposit them at considerable distances from their initial location, (Constantinescu, 2014). The control of gravity current propagation during the demolition stages of a dam has increasingly gained importance (Papanicolaou and Barkdoll, 2011), and little is understood about its erosion capacity under controlled releases. Additionally, the presence of entrained bed material in the body of the current may alter the dynamic of the current itself, accelerating or decelerating the propagation of the front. A proper understanding of such phenomena, especially for salinity currents formed in estuaries, can help in the mitigation of environmental impacts such as inundation of mangrove ecosystems, water quality and sedimentary processes. However, our knowledge is still limited regarding the interactions between fluid processes and sediment dynamics.

The erosion and deposition phenomena that arise from the interaction of gravity currents with the bed, have been mainly investigated on turbidity currents over the last few years. Akiyama and Stefan (1986) and Parker et al. (1986) have proposed an analytical model that describes the propagation of turbidity currents taking into account the water entrainment in the current body from above, as well as the sediment exchange between the turbidity current and the bed. Parker et al. (1987) conducted laboratory experiments of turbidity currents flowing above an erodible bed which consists of sediment similar to that carried by the current itself. The velocity and concentration profiles were studied to evaluate the water and sediment entrainment coefficients of the governing equations. In Necker et al. (2002) high-resolution numerical simulations were performed to investigate the sedimentation process in particle-driven gravity currents as well as the influence of particle settling on the dynamics of the flow. They observed that during the early stages of the current the mass flux of sedimenting particles increases, but when the half of the particles have been already settled out, the mass flux rapidly decreases. Besides, they mentioned the possibility of particles resuspension and addressed the particle Reynolds number and the shear velocity as governing parameters. Finally, the sediment transport induced by turbidity currents along with the influence of bed forms on velocity and density profiles have been investigated by Sequeiros et al. (2010a, 2010b).

The peculiarity of the studies on turbidity currents, such as those mentioned above, is that the source of buoyancy difference, i.e. the suspended sediment, consists of a material similar to that of the bed. Therefore, the estimation of the net flux of bed material entrainment is an issue that remains difficult to overcome. To address the bed material entrainment and its influence in the dynamics of the gravity currents, salinity currents are generally studied. Salinity currents are conservative with respect to the agent that drives the flow and they are a good analogue to weakly depositional turbidity currents (Cossu and Wells, 2012). Garcia and Parker (1993) conducted pioneering experiments of salinity currents flowing downslope over a mobile bed to analyze the entrainment capacity. They observed that conservative currents with a large excess of density can entrain a large amount of bed material into suspension. Additionally, they reported an empirical relation for the entrainment of sediment in suspension, as a function of the bottom shear stress, grain size, and other parameters related with the flow dynamics and the characteristics of the bed material. Eames et al. (2001) developed a mathematical model able to reproduce the resuspension induced by saline and particle-driven currents, combining the knowledge of buoyancy-driven flows and of resuspension in steady channel flows.

The spatial and the temporal distribution of the bed shear stress are key parameters for estimating sediment entrainment, which in turn require the instantaneous measurement of velocity in the viscous sublayer at the bottom of the current. This information is generally difficult to obtain in laboratory due to the fact that the boundary layer constitutes only a small fraction of the total flow depth (Cossu and Wells, 2012). However, high-resolution numerical simulations can provide it, together with a physical insight of the correlation between the turbulent structures generated in the proximity of the wall and the sediment entrainment.

Direct Numerical Simulations (DNS) resolve all the relevant scales in the flow down to the dissipative range and have been widely used to study gravity currents. However, their application is limited to low Reynolds numbers and simple geometries due to high computational cost (e.g. Härtel et al., 2000a; Härtel et al., 2000b; Necker et al., 2005). Large Eddy Simulations (LES) have recently emerged as an appropriate tool for the study of gravity currents (Constantinescu, 2014). In LES the dissipative scales which are assumed isotropic and do not depend on the geometry scales of the model, are modeled by a sub-grid scale (SGS) model. Therefore, this approach makes LES more adequate to study gravity currents at high Reynolds numbers. A LES simulation of lock-exchange compositional currents over a flat bed was reported by Ooi et al. (2009), who studied compositional gravity currents with small initial volume of release. They investigated the effect of the Reynolds number on the near-bed flow structure and on the bed friction velocity distributions induced by the passage of a gravity current after the bore was formed. They also concluded that the sediment entrainment increases, rising the Reynolds number of the current. However, they did not consider particles entrainment. This aspect is crucial to asses how suspended sediment can alter the buoyancy of the current and affect the propagation of the front, causing, for example, a self-accelerating effect. Additionally, by considering particle entrainment and transport in the mathematical model allows to quantify the amount of the eroded material, and investigate the distal transport and the deposition of sediment. These phenomena are related with some of the environmental hazards mentioned above such as pollutant dispersion and reservoir sedimentation.

In the present work a 3D LES model by Roman et al. (2010) is used to perform numerical simulations of full-depth salinity currents at high Reynolds numbers flowing over a mobile bed. The simulated currents are driven by small density differences (less than (4%)), so that the Boussinesq approximation is considered true. Our overall goal is to define an appropriate formulation, concerning the erosion and the deposition rate of the suspended sediment, to numerically reproduce the entrainment and transport of particles induced by the passage of the current above the mobile bed. The numerical results of the current simulation are compared with experimental data provided by an equivalent experimental study. The second aim is to correlate the flow properties with the entrainment processes and to point out the control mechanisms of erosion. We also aim at identifying the regions of the current that are the most active in terms of erosion. Furthermore, the numerical simulations are able to provide a better insight than the experiments, regarding the effect of the entrained material on the dynamics of the gravity current. Finally, the importance of the

stratification on the suspended sediment distribution is also investigated. Three different current Grashof numbers and two different bed grain sizes have been reproduced numerically.

The paper is organized as follows. First the study case is presented in Section 2 followed by the description of the problem formulation and the numerical model in Section 3. The main characteristics of the current are illustrated in Section 4. In the same section the velocity fields and the estimated bed shear stress are discussed. The analysis of the sediment entrainment induced by the passage of the salinity current above the mobile bed is presented in Section 5.1, and the numerical results are compared with experimental data. The correlations between the flow properties and the sediment entrainment are shown and discussed in Section 5.3. Finally, Section 6 summarizes the main conclusions.

2. Description of study case

The set-up of the numerical simulations considered in the present work is inspired by the experimental study of Zordan et al. (2017), which investigates experimentally the propagation of a salinity current over a mobile bed. The laboratory set-up consists of a rectangular flume 7.48 m long, 0.2 m deep, and 0.275 m wide with downstream tank for the dissipation of the current. The horizontal flume is composed by two volumes of fluid with different densities due to salinity differences, separated by a movable lock-gate at a distance $x_0 = 2.5$ m form the rear wall. Moreover, a mobile bed 0.6 m long is located at distance 2.5 m from the gate. The instantaneous flow velocities, exactly before the mobile section of the bed, have been measured in the experiments using the 3D Acoustic Doppler Velocity Profiler (ADVP) (Franca and Lemmin, 2006; Lemmin and Rolland, 1997). The rapid removal of the vertical gate in the experimental work may add some disturbances at the initial stages of the generated flow. However, the velocity measurements have been recorded far enough from the lock so they can be considered independent of the gate opening speed. Additionally, a high-speed camera SMX-160 has recorded the evolution of the current and the bed material entrainment as the current propagates above the mobile reach of the bed.

The numerical set-up reproduces the rectangular flume. To allow the current dissipation a 10.0 m long extra part is added downstream. The additional part of the flume ensures that, the obtained results are not disturbed by the reflection of the gravity current at the end of the flume and return flow is not present. The initial aspect ratio of the lock fluid $R = H/x_0 = 0.08 << 1$ (where H is the height of the flume) is kept constant. A conceptual model of the numerical set up along with the mesh details is given in Fig. 1.

In this paper two salinity currents, namely test - A/B and C/D -, are simulated taking into account different initial salinity concentrations (C^1_{sal}) of the fluid in the lock. The changes of initial salinity concentrations (C^1_{sal}) are modeled numerical by adapting the Grashof number:

$$\mathrm{Gr} = \left(\frac{u_b H}{\nu}\right)^2, \tag{1}$$

which is calculated with respect to the kinematic viscosity of the fluid ν, the buoyancy velocity of the current, u_b and the height of the flume

$$u_b = \sqrt{g' H}, \tag{2}$$

where

$$g' = g\frac{\rho_{lock} - \rho_w}{\rho_w}, \tag{3}$$

and ρ_{lock} is the density at the lock. The ambient fluid volume beyond the lock has always zero-initial salinity (C^0_{sal}) and density ρ_w. The density of the current can be calculated by the state equation

$$\rho = \rho_w\left[1 + \beta\left(C_{sal} - C^0_{sal}\right)\right], \tag{4}$$

where C_{sal} represents the salinity concentration at each point and β is the salinity contraction coefficient whose value can be found in IOC et al. (2010).

The main features of the current, front velocity and current shape, are validated and the velocity and bed shear stress distributions are studied for different Grashof numbers. The evolution of the front for simulations A/B and C/D and the shape of the current for simulations A/B and C/D, are presented in the following sections and compared with experimental data obtained in the study of Zordan et al. (2017). The velocity of the current has been recorded on an Eulerian frame (probe), located in the middle of the channel in the spanwise direction, exactly before the mobile section of the bed, at distance $x = 2.5$ m from the lock (see Fig. 1).

Finally, the importance of the sediment size is investigated by simulating two different grain sizes. More specifically, in cases A and C the bed consists of finer sediment than those used in cases B and D. The sediment used in the experiments is non-cohesive High-Performance Thermoplastic Polyurethane (TPU) with mass density equal to $\rho_s = 1160$ kg/m^3. In the numerical simulations the different grain sizes are implemented by modifying the critical Shields parameter (θ_{cr}) and the settling velocity (w_s).

It is worth noting that the dynamics of the current have been studied upstream the mobile bed. A detailed description of the simulation parameters is presented in Table 1. The non-dimensional grain size d^+ is defined as:

$$d^+ = \frac{d u_*}{\nu}, \tag{5}$$

where d is the median sediment diameter (d_{50}), and u_* represents the maximum bed shear velocity recorded at the probe before the mobile bed.

The bed material chosen in this work is expected to be transported directly into suspension since $w_s/u_* < 1$ (Van Rijn, 1984). The behavior of the sediment in suspension can be characterized

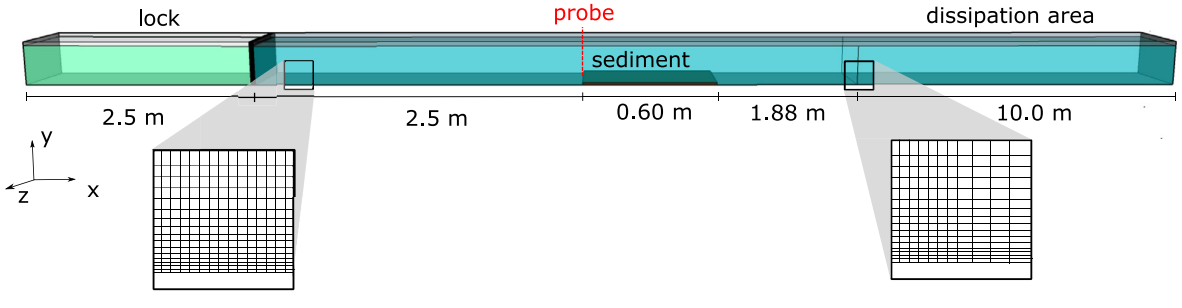

Fig. 1. Conceptual model of the study case and mesh details (not scaled). The mesh at the dissipation part is coarser compared to the mesh of the rectangular flume.

Table 1
Parameters of the lock-exchange simulations.

Test	ρ_{lock} [kg/m^3]	g' [m/s^2]	u_b [m/s]	$\sqrt{Gr}$ [–]	d [m]	u_* [m/s]	d^+ [–]	θ_{cr} [–]	w_s [m/s]
A	1040	0.39	0.28	56,000	80×10^{-6}	0.014	1.10	0.15	5.5×10^{-4}
B	1040	0.39	0.28	56,000	150×10^{-6}	0.014	2.10	0.09	17.4×10^{-4}
C	1048	0.47	0.31	61,000	80×10^{-6}	0.012	1.00	0.15	5.5×10^{-4}
D	1048	0.47	0.31	61,000	150×10^{-6}	0.012	1.80	0.09	17.4×10^{-4}

Table 2
Estimated Stoke numbers for all the cases studied in this work.

Test	η [m]	St_d [–]
A	5.5×10^{-5}	0.11
B	5.5×10^{-5}	0.12
C	5.1×10^{-5}	0.24
D	5.1×10^{-5}	0.27

by the Stokes number of the particle, which expresses the ratio of the response time of a particle $\tau_p = (1/18)(\rho_s/\rho_w)(d^2/\nu)$ to the turbulent dynamic time at the scale of the particle size $\tau_d = (d^2/\epsilon)^{1/3}$ (Mattioli et al., 2012). In particular, Stokes number higher than 1 indicates that, the particles detach from the flow whereas for Stokes number lower than 1, particles follow closely the fluid streamlines. The Stokes number can be defined as,

$$St_d = \frac{\tau_p}{\tau_d} = (1/18)(\rho_s/\rho_w)(d^2/\eta^{4/3}), \tag{6}$$

where η is the Kolmogorov lengthscale equal to $(\nu^3/\epsilon)^{1/3}$ and ϵ is the turbulent dissipation rate. The calculated Stokes numbers, are presented in Table 2. These values show that, for all the cases considered here the particles are following closely the flow. This justifies, the use of the Euler-Euler single phase approach for modeling the evolution of the entrained material.

3. Mathematical and numerical model

The numerical tool used in this work is LES-COAST, a code presented in Roman et al. (2010) and successive papers. The suspended sediment is treated as a scalar field, since a single-grain resolution approach is impractical for the case in analysis (Leonardi et al., 2015). Therefore, the model solves the filtered Navier–Stokes equations together with two scalar transport equations, one for salinity and one for sediment concentration. The Adams–Bashforth technique is used for the time evolution of the convective terms, whereas the diffusive terms are treated implicitly with the Crank–Nicolson scheme. The space derivatives are discretized with a second-order centered scheme, except for the advective terms which are discretized using a third-order accurate, upwind scheme (Quick, Leonard (1979)). A multigrid technique is used for the solution of the pressure equation. This model has been validated over the past years for similar flows, e.g. Dallali and Armenio (2015), Ottolenghi et al. (2016a, 2016b, 2017a).

With the LES technique, the governing equations of the flow are filtered (filtered variables are denoted by [$\bar{}$]) and the large, anisotropic scales of motion are explicitly solved while the small, isotropic and dissipative scales are modeled using a subgrid-scale (SGS) model. As mentioned above, the density difference between the lock and the ambient fluid is small enough to admit the Boussinesq assumption as valid. Consequently, density can be treated as constant in the momentum equation with the exception of the body force terms. The filtered continuity and momentum are presented below:

$$\frac{\partial \bar{u}_i}{\partial x_i} = 0, \tag{7}$$

$$\frac{\partial \bar{u}_i}{\partial t} + \frac{\partial \bar{u}_j \partial \bar{u}_i}{\partial x_j} = -\frac{1}{\rho_w}\frac{\partial \bar{p}}{\partial x_i} + \nu \frac{\partial^2 \bar{u}_i}{\partial x_j \partial x_j} - \frac{\Delta\rho}{\rho_w} g \delta_{i,2} - \frac{\partial \tau_{ij}}{\partial x_j}, \tag{8}$$

The quantities $\bar{p}$ and $\bar{u}_i$ denote the filtered pressure and the filtered velocity components in the x_i direction of the computational domain. Moreover, $\Delta\rho$ denotes the density variation due to salinity and sediment concentration defined as,

$$\frac{\Delta\rho}{\rho_w} = \frac{\rho - \rho_w}{\rho_w} = \beta \bar{C}_{sal} + s\bar{C}_{sed}, \tag{9}$$

where C_{sal} is salinity, C_{sed} the sediment concentration, and $s = \frac{\rho_s - \rho_w}{\rho_w}$ is the buoyant density of the sediment. Indexes i=1,2,3 correspond to the streamwise, vertical, and spanwise direction, respectively. Here after, streamwise, vertical, and spanwise directions are also denoted by *x*, *y*, and *z*, respectively. Similarly, u_1, u_2, and u_3 are also referred as *u*, *v*, and *w*. The effects of the smaller scales in the momentum equation are contained in the term:

$$\tau_{ij} = -2\nu_t \bar{S}_{ij}, \tag{10}$$

where the large scale strain rate tensor S_{ij} is equal to:

$$\bar{S}_{ij} = \frac{1}{2}\left(\frac{\partial \bar{u}_i}{\partial x_j} + \frac{\partial \bar{u}_j}{\partial x_i}\right) \tag{11}$$

and the eddy viscosity is defined as,

$$\nu_t = (C_s \Delta)^2 |\bar{S}|, \tag{12}$$

where C_s is the Smagorinsky coefficient and Δ represents the filter width used in LES technique. In this work, the Smagorinsky coefficient has been calculated using the Lagrangian dynamic SGS model described in Meneveau et al. (1996). In this approach, the values of C_s are not set *a priori* as in the standard Smagorinsky model, but are rather estimated locally from the resolved velocity field of LES. The noteworthy feature of the Lagrangian model is that, the required averages (see Lilly, 1992) are made along fluid pathlines. This is important, for inhomogeneous flows like the one simulated in this work.

For the spatio-temporal evolution of salinity and sediment concentration two scalar transport equations are used:

$$\frac{\partial \bar{C}_{sal}}{\partial t} + \frac{\partial \bar{u}_j \bar{C}_{sal}}{\partial x_j} = \kappa_{sal} \frac{\partial^2 \bar{C}_{sal}}{\partial x_j \partial x_j} - \frac{\partial \lambda_j}{\partial x_j}, \tag{13}$$

$$\frac{\partial \bar{C}_{sed}}{\partial t} + \frac{\partial (\bar{u}_j - w_s \delta_{i,2}) \bar{C}_{sed}}{\partial x_j} = \kappa_{sed} \frac{\partial^2 \bar{C}_{sed}}{\partial x_j \partial x_j} - \frac{\partial \eta_j}{\partial x_j}, \tag{14}$$

where

$$\lambda_j = -\kappa_{t,sal} \frac{\partial \bar{C}_{sal}}{\partial x_j}, \tag{15}$$

$$\eta_j = -\kappa_{t,sed} \frac{\partial \bar{C}_{sed}}{\partial x_j}. \tag{16}$$

The quantity κ_{sal} is the molecular salt diffusivity, and κ_{sed} the molecular diffusivity of sediment. The eddy diffusivity, κ_t, for both

salt and sediment, is related to the eddy viscosity by the SGS Schmidt number,

$$\mathrm{Sc}_{\mathrm{SGS}} = \frac{\nu_\mathrm{t}}{\kappa_\mathrm{t}}. \tag{17}$$

The momentum, and the two above scalar equations have been made dimensionless using the height of the channel H and the buoyancy velocity u_b as follows:

$$\frac{\partial \hat{\tilde{u}}_i}{\partial \hat{t}} + \frac{\partial \hat{\tilde{u}}_j \partial \hat{\tilde{u}}_i}{\partial \hat{x}_j} = -\frac{\partial \hat{\tilde{p}}}{\partial \hat{x}_i} + \frac{1}{\sqrt{\mathrm{Gr}}} \frac{\partial^2 \hat{\tilde{u}}_i}{\partial \hat{x}_j \partial \hat{x}_j} - \frac{\Delta\rho}{\rho_\mathrm{lock} - \rho_\mathrm{w}} \delta_{i,2} - \frac{\partial \hat{\tau}_{ij}}{\partial \hat{x}_j}, \tag{18}$$

$$\frac{\partial \bar{C}_\mathrm{sal}}{\partial \hat{t}} + \frac{\partial \hat{\tilde{u}}_j \bar{C}_\mathrm{sal}}{\partial \hat{x}_j} = \frac{1}{\sqrt{\mathrm{Gr}}\mathrm{Sc}_\mathrm{sal}} \frac{\partial^2 \bar{C}_\mathrm{sal}}{\partial \hat{x}_j \partial \hat{x}_j} - \frac{\partial \hat{\lambda}_j}{\partial \hat{x}_j}, \tag{19}$$

$$\frac{\partial \bar{C}_\mathrm{sed}}{\partial \hat{t}} + \frac{\partial (\hat{\tilde{u}}_j - \hat{w}_\mathrm{s}\delta_{i,2})\bar{C}_\mathrm{sed}}{\partial \hat{x}_j} = \frac{1}{\sqrt{\mathrm{Gr}}\mathrm{Sc}_\mathrm{sed}} \frac{\partial^2 \bar{C}_\mathrm{sed}}{\partial \hat{x}_j \partial \hat{x}_j} - \frac{\partial \hat{\eta}_j}{\partial \hat{x}_j}, \tag{20}$$

where the symbol [^] denotes the dimensionless quantities. The Schmidt numbers (Sc_sal and Sc_sed) are the ratio of the molecular viscosity ν to the molecular diffusivities of the scalars (κ_sal and κ_sed). For salinity, Sc_{sal} is equal to 600 and for sediment Sc_{sed} is equal to 1. In the dimensionless form of the momentum equation, the density variation due to salinity and the presence of suspended particles is equal to:

$$\frac{\Delta\rho}{\rho_\mathrm{lock} - \rho_\mathrm{w}} = \frac{\rho - \rho_\mathrm{w}}{\rho_\mathrm{lock} - \rho_\mathrm{w}} = \frac{\bar{C}_\mathrm{sal}}{\bar{C}^1_\mathrm{sal}} + \frac{s}{\beta \bar{C}^1_\mathrm{sal}} \bar{C}_\mathrm{sed}. \tag{21}$$

The dimensions of the scaled domain are $L_1 = 87.4H$, $L_2 = H$, $L_3 = 1.375H$. However, only a length of $37.4H$ in x is used for data analysis omitting the part which serves for the dissipation of the current. The computational grid is composed of $1336 \times 128 \times 80$ cells in the main domain and 200 additional cells, gradually enlarged in the streamwise direction, for the region of the channel where the current is dissipated (see Fig 1). Stretching has been applied on the vertical and spanwise directions following Vinokur's algorithm which uses an hyperbolic tangent law (Vinokur, 1983). The grid spacing in the vicinity of the bottom and of the lateral walls is chosen to be equal to $\Delta z = \Delta y = 0.0005H$ in order to fully resolve the viscous sublayer. These values, in wall units, give $\Delta y^+ = (u_*/\nu)\Delta y = 1$ and $\Delta z^+ = (u_*/\nu)\Delta z = 1$. Away from the wall the grid spacing is equal to $0.01H - 0.04H$, similar to the one adopted in Ooi et al. (2009) for high Grashof number gravity current.

A no-slip boundary condition is set at the walls in the spanwise and streamwise directions, as well as at the bottom of the channel. At the top surface of the flume a free-slip boundary condition is applied. Concerning salinity, a zero normal gradient is imposed at each boundary.

3.1. Sediment pick-up

The passage of the current above the mobile section of the bed can lead to the entrainment of the particles, which can then be carried in suspension or deposited downstream. The exchange of sediment between the bed and the current is reproduced numerically by imposing the sediment fluxes to be dependent on the erosion and sedimentation rate as in Kraft et al. (2011), hence imposing the boundary condition:

$$\left(\frac{1}{\sqrt{\mathrm{Gr}}\mathrm{Sc}_\mathrm{sed}} grad \bar{C}_\mathrm{sed} \cdot e_2 + w_\mathrm{s} \bar{C}_\mathrm{sed} \right) = S - \frac{E}{\rho_\mathrm{s}}, \tag{22}$$

where e_2 is a unit vector in the direction of gravity and the symbol $(\cdot)$ represents the scalar product. Moreover, S stands for the sedimentation rate and E represents the erosion rate.

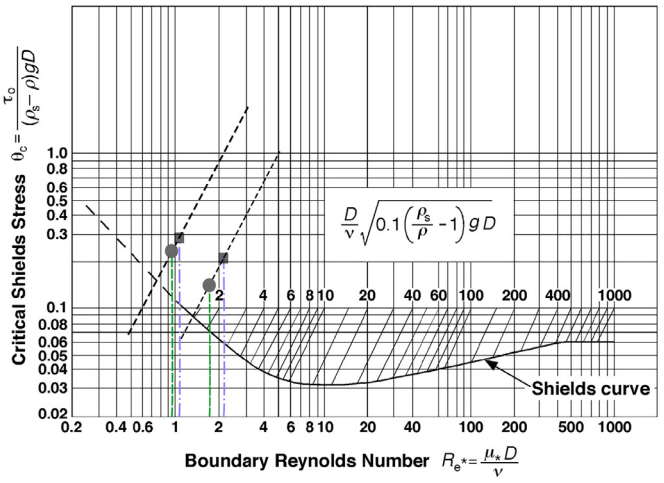

Fig. 2. Shields diagram as modified by Vanoni (1975). The squares indicate the position of $d^+ = 1.1$ and $d^+ = 2.1$ for cases *A* and *B*, whereas circles represents the position of $d^+ = 1.00$ and $d^+ = 1.80$ for cases *C* and *D*. The inclined dashed lines represent the values of Vanoni's dimensionless parameter for each diameter.

The incipient motion of sediment occurs when the dimensionless bed shear stress, $\theta = \tau_\mathrm{w}/(\rho_\mathrm{s} - \rho_\mathrm{w})gd$, exceeds a critical value, θ_cr, that depends on the bed material and on the flow conditions. In this work, the values of critical bed shear stress are estimated using the Shields diagram as modified by Vanoni (1975). More specifically, Vanoni introduced an extra dimensionless parameter V_s (see Eq. (23)), which extends the Shields diagram to suspended sediment, and corresponds to a group of parallel inclined lines. The intersection between those lines and the Shields curve provides the value of the critical shear stress, τ_cr (see Fig. 2):

$$V_s = \frac{d}{\nu}\sqrt{0.1sgd}, \tag{23}$$

After the threshold for the initiation of motion is calculated, an additional equation is required to determine the amount of eroded particles, E. In the literature many different pick-up formulations can been found. In the present work, the approach introduced by Fernandez Luque and Van Beek (1976) is used. This approach is adequate for particle diameter $d < 200\,\mu$m which was the case in the experiments from Zordan et al. (2017). Luque (Fernandez Luque and Van Beek, 1976) assumes that the erosion rate is an exponential function of the sediment diameter, buoyant weight, and of the distance of the Shields parameter from its critical value (see Eq. (24)).

$$E = \alpha \rho_\mathrm{s} (sgd)^{0.5} (\theta - \theta_\mathrm{cr})^{1.5}, \tag{24}$$

The empirical constant α has to be defined experimentally. According to van Rijn (1984), the empirical constant in Luque's approach (Fernandez Luque and Van Beek, 1976) is equal to $\alpha = 0.02$ for spherical particles as those used in the experiments by Zordan et al. (2017).

Finally, an important parameter that influences the suspended sediment transport as well as their deposition is the settling velocity. For sediment diameters in the range of $100 - 1000\ \mu$m, as those that have been considered in the present paper, the settling velocity can be computed using Zanke's approach (Zanke, 1977):

$$w_\mathrm{s} = \frac{10\nu}{d}\left[\left(1 + \frac{0.01sgd^3}{\nu^2} \right)^{0.5} - 1 \right]. \tag{25}$$

The deposition rate of the suspended sediment is then equal to:

$$S = w_\mathrm{s} C_\mathrm{ref}, \tag{26}$$

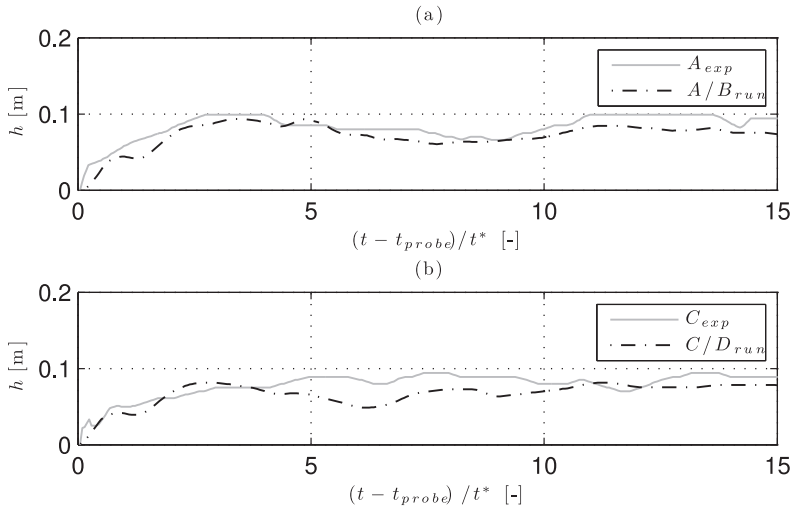

Fig. 3. Representation of the current height. The numerical results (dashed line) are compared with experimental results (solid lines): (a) corresponds to $\sqrt{\mathrm{Gr}} = 56000$; (b) to $\sqrt{\mathrm{Gr}} = 61000$.

where C_{ref} corresponds to the sediment concentration in the immediate vicinity of the bottom, which is numerically represented by the first grid point away from the wall.

4. Characterization of the gravity current

In this section the hydrodynamics of the current before the mobile reach of the bed are presented. Additionally the front velocity of the current has been calculated, upstream and above the mobile section of the bed. The numerical simulations have been compared with available experimental data, in terms of current height and front evolution.

4.1. Current height

With the removal of the lock-gate the heavier fluid forms a current, which propagates over the bottom of the flume with positive velocity while the ambient fluid forms a counter-current flowing in the opposite direction in the upper part of the flume. In the literature are reported two ways to define the interface between the current and the counter-current, which coincides with the height of the current. The first approach uses, as threshold, the density of the current (Ottolenghi et al., 2016a), whereas according to the second approach the interface can be defined as the position where the streamwise velocity changes sign. In the comparisons of Figs. 10 and 11 where the experimental results have been derived by video and image analysis, the first approach is the most adequate to define the current shape. However, to compare the height of the current estimated upstream the mobile bed, where only velocity measurements are available in the experimental work, the second approach is used.

Here, the spatial visualization of the shape of the current can be retrieved by the time series of velocity measurements assuming that the frozen turbulence hypothesis holds true, and that the current is advected at nearly constant velocity. The time evolution of the current height h for the numerical simulations $A|B$ and $C|D$, compared with the height recorded in the laboratory experiments, is presented in Fig. 3. In the experimental work, the detection of the contour with the ADVP has a precision of $+-4.5$ mm. In fact, the instrument records at 44 equally spaced positions along the vertical which means that the total fluid height of 200 mm is divided in 44 gates of about 4.5 mm each. The detection of the zero-velocity height is therefore within this interval of error. The comparison of the numerical simulations outcome with the experimental data should be done in a qualitative sense, since the estimation of the current height in the experiments is based on instantaneous velocity measurements in a specific probe. The upper boundary is distinguished, both numerically and experimentally, as the iso-velocity contour at $u = 0.01$ m/s of the velocity measurements obtained at the Eulerian frame presented in Fig. 1. t_{probe} represents the time instant when the current arrives at the probe and t^* represents the time scale h/u_{b} that is used to make the time dimensionless. The current height varies between $0.06\,\mathrm{m} < h < 0.1\,\mathrm{m}$ and seems to be slightly influenced by the change of the Grashof number (i.e. the buoyancy of the current itself). The shape of the current is not influenced by the presence of the sediment since the measurements have been done when the current passes by a probe located before the mobile section of the bed. The head of the current, where a stronger mixing is observed, can be roughly defined as the region below the h curve, until the first local minimum that appears after the max value. This minimum, for both cases studied here, can be observed around $(t - t_{\mathrm{probe}})/t^* = 5$. The remaining area corresponds to the body of the current.

4.2. Front position

The instantaneous front position, $x_{\mathrm{f}} = x - x_{\mathrm{lock}}$, for cases B and D is numerically calculated by identifying the streamwise position of the foremost point of the current in a plane located at distance $y = 0.1H$ from the bottom, as in Ooi et al. (2009). These results are presented in Fig. 4. It is noteworthy that, hereafter the boundary of the current is deduced from the density contours and not from the velocity measurements for the reasons presented in the previous section. The non-dimensional iso-density contour $(\rho - \rho_{\mathrm{lock}})/(\rho_{\mathrm{lock}} - \rho_{\mathrm{w}}) = 0.02$ is chosen asthose of Ottolenghi et al. (2016a). The evolution of the front over time shows that, when the current passes over the mobile bed (for $x_{\mathrm{f}} = 2.7$ to $x_{\mathrm{f}} = 2.95$), the presence of suspended sediment is not strong enough to significantly influence the propagation of the front. This means that the propagation of the front for the cases A and C, is the same as the one of cases B and D, respectively. The influence of the suspended sediment in the dynamics of the current is studied in more detail in the following sections. The numerical values of x_{f} along with the corresponding experimental data are plotted in Fig. 4 showing good agreement. It has to be mentioned here that the identification of the current limit in the experimental work is carried out by subtracting an initial image of an interrogation window with ambient fluid from the images

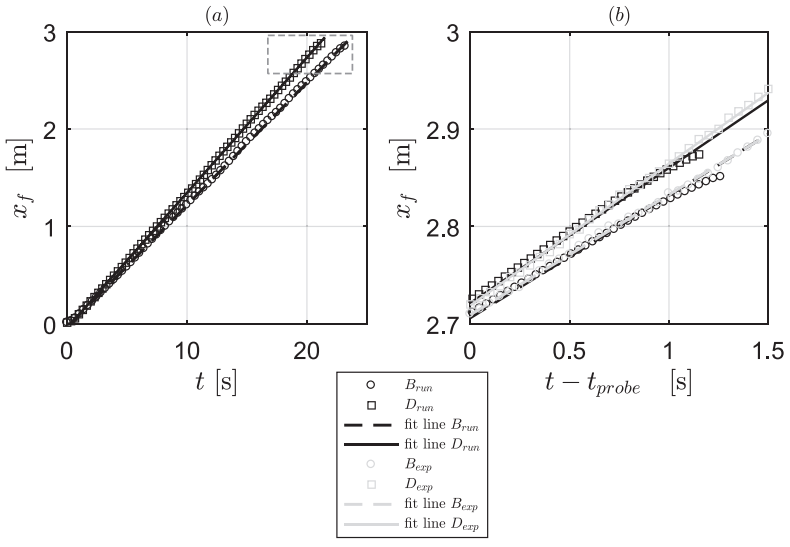

Fig. 4. (a) Time evolution of the distance between the front and the lock for cases *B* and *D*. The dashed square indicates the time period that the current propagates above the mobile reach of the bed. (b) Time evolution of the front position above the mobile reach of the bed and comparison of numerical results with experimental data. t_{probe} indicates the time instant that the current arrives at the probe.

of the experiments. The flow regions (current and sediment) can be thus separated by sharp interfaces, and ultimately, they can be identified. The precision in the identification of the sharp images is of the order magnitude of the pixel resolution, i.e., 0.5 mm/pixel. The effect of the increasing Grashof number on the propagation of the current becomes evident by the increased slope of line $x_f(t)$ for *D* compared to *B*. The linear trend of the front position as presented in Fig. 4 proves that the current is in the slumping phase, where according to literature (Huppert and Simpson, 1980; Ooi et al., 2009) the front velocity $u_{\text{front}} = \mathrm{d}x_f/\mathrm{d}t$ remains constant.

The front velocity of the current can be also expressed using a Froude number, defined as:

$$\mathrm{Fr} = \frac{u_{\text{front}}}{u_b}. \tag{27}$$

The calculated averaged front velocities, u_{front}, as well as the Froude number, Fr, for cases *A*/*B* and *C*/*D* are presented in Table 3. The Froude number expresses the ratio between the inertia of the fluid and the buoyancy forces driving the current, and its value lies in the range of 0.45 ± 0.05, in accordance with the values reported in the literature for similar cases (Benjamin, 1967; Nogueira et al., 2013). Such values indicate that all the currents are subcritical. This justifies the use of the non-deformable slip boundary condition on the top of the flume. Furthermore, it can be observed that an increase in the Grashof number of the order of 8–10% leads to a Froude number increase of approximately 2–3%.

Table 3
Froude numbers, calculated based on the channel height, for the two different Grashof numbers.

Test	$\sqrt{\mathrm{Gr}}$	u_{front} [m/s]	u_b [m/s]	Fr
A/B	56,000	0.125	0.28	0.46
C/D	61,000	0.14	0.31	0.45

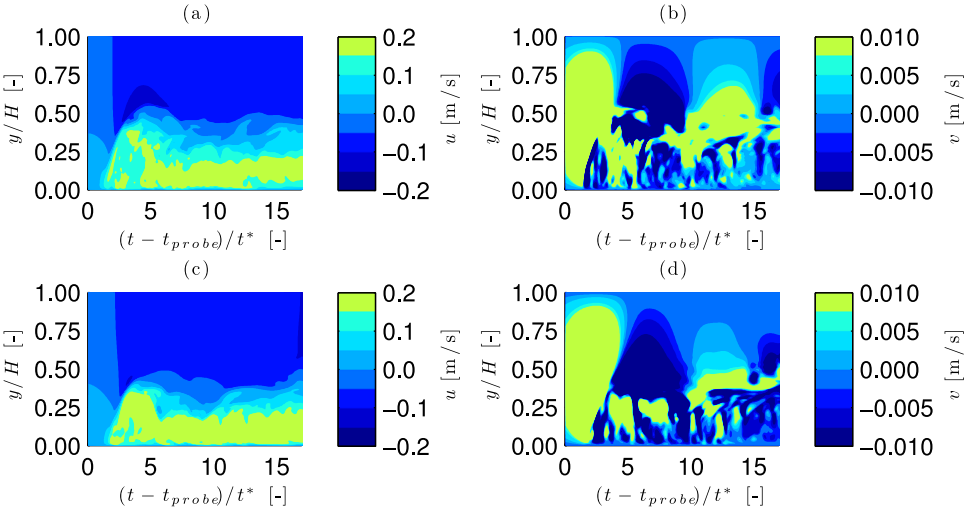

Fig. 5. Numerical results of the instantaneous velocity contours. The measurements are taken in the Eulerian frame at the middle of the channel before the mobile section of the bed. The time is made dimensionless using $t^* = H/u_b$. Plots (a) and (b) represent the streamwise and vertical velocities for $\sqrt{\mathrm{Gr}} = 56000$, and (c) and (d) for $\sqrt{\mathrm{Gr}} = 61000$.

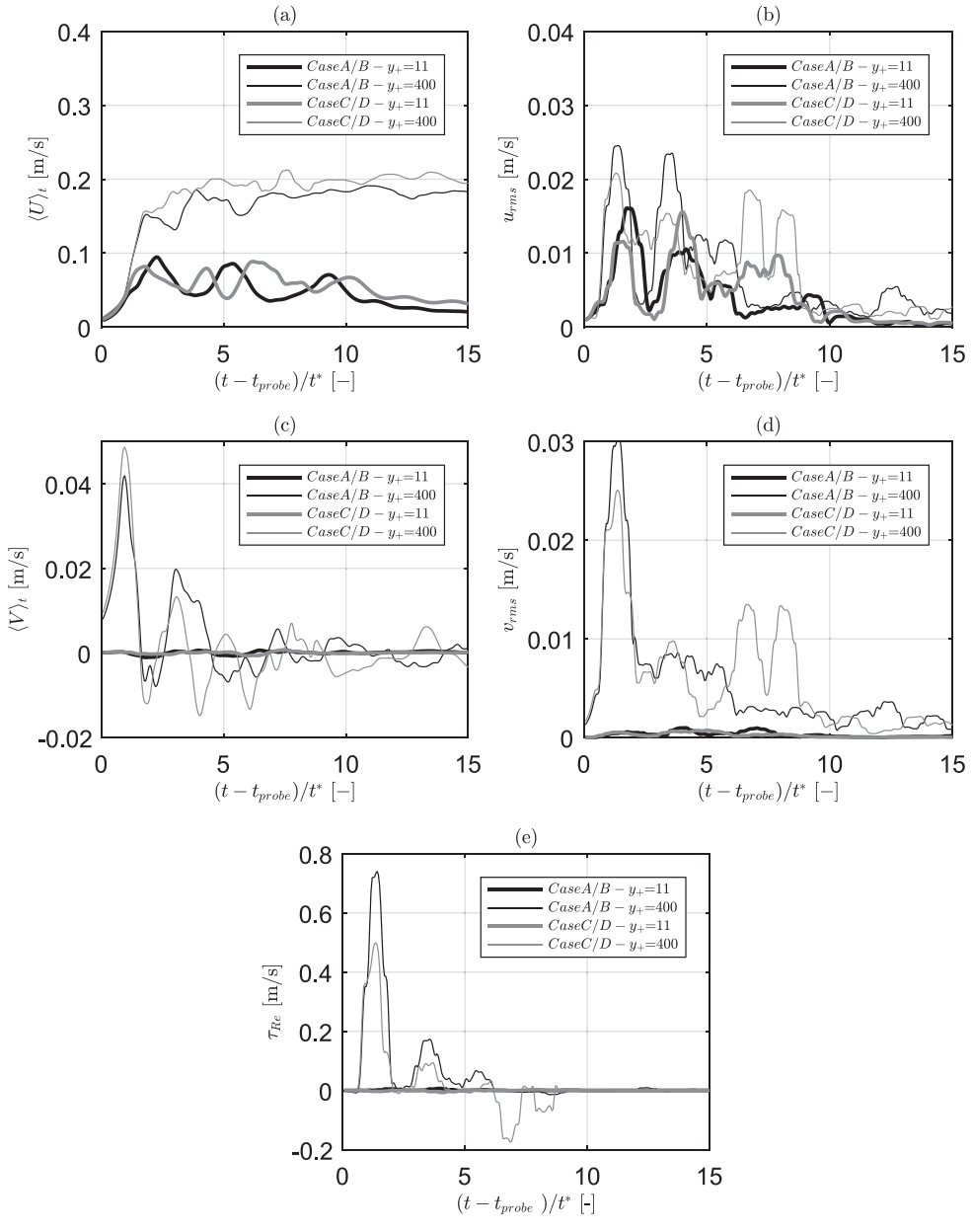

Fig. 6. Time evolution of the (a) time averaged streamwise velocity $\langle U \rangle_t$, (b) streamwise velocity fluctuations u_{rms}, (c) time averaged vertical velocity $\langle V \rangle_t$, (d) vertical velocity fluctuations v_{rms}, and (e) Reynold shear stresses τ_{Re} at two different heights for $\sqrt{\mathrm{Gr}} = 56000$, and $\sqrt{\mathrm{Gr}} = 61000$.

4.3. Current dynamics

The numerically calculated instantaneous contour plots of the streamwise and vertical velocities, for all cases, are presented in Fig. 5. As mentioned before, the values are measured as the current crosses a probe station located at distance $x = 2.5$ m from the lock at the middle of the channel, just upstream of the mobile bed (see Fig. 1). In the lower half of the channel, positive streamwise velocities are observed that corresponds to the propagation of the dense fluid. In the upper part, the streamwise velocities are negative indicating the movement of the ambient fluid in the opposite direction. This velocity difference across the interface between the two fluids leads to the creation of a shear layer and continuously to instabilities. Furthermore, regarding the vertical velocities, a high positive value is registered ahead of the arrival of the front current. This value represents the upwards displacement of the ambient fluid by the dense current. The ambient fluid is then moved downwards towards the body of the current (drop of V). A similar pattern, characterized by a sequence of upward and downward fluxes, is followed on the whole mixing area behind the head. It is assumed that, these features will have an effect on the entrainment of bed material and will be discussed subsequently.

The instantaneous velocity measurements, presented above, have been used to calculate a time running average of the horizontal and vertical velocity of the current, $\langle U \rangle_{\mathrm{t}}$ and $\langle V \rangle_{\mathrm{t}}$ in the height of the current. For the averaged quantities a $(t - t_{\mathrm{probe}})/t^* = 0.7$ time window is chosen according to Baas et al. (2005). The time window corresponds to 16 velocity recordings and is chosen to avoid filtering out the small-frequency peaks. To investigate the turbulent velocity components the root mean square of the velocity fluctuations, u_{rms} and v_{rms} are computed as,

$$u_{\mathrm{rms}}(y) = \sqrt{\langle u'^2 \rangle_{\mathrm{t}}(y)} = \left[\frac{1}{n} \sum_{m=1}^{n} \left[u_{\mathrm{m}}(y) - \langle U \rangle_{\mathrm{t}}(y) \right]^2 \right]^{0.5}, \qquad (28)$$

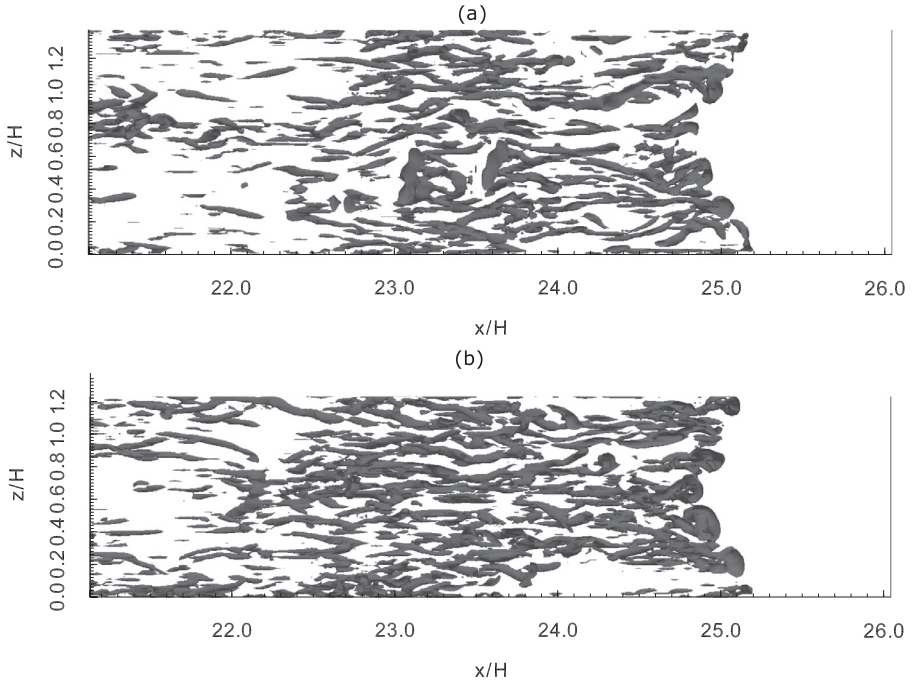

Fig. 7. Top view of the isosurface $\lambda_2 = -200$ at wall turbulent layer, at time instant $(t - t_{\text{probe}})/t^* = 0$. Only the region near the front is displayed. (a) $\sqrt{\text{Gr}} = 56000$ (b) $\sqrt{\text{Gr}} = 61000$.

$$v_{\text{rms}}(y) = \sqrt{\langle v'^2 \rangle_{\text{t}}(y)} = \left[\frac{1}{n} \sum_{m=1}^{n} \left[v_{\text{m}}(y) - \langle V \rangle_{\text{t}}(y) \right]^2 \right]^{0.5}, \tag{29}$$

where n represents the number of points used for the time average, and u_m, v_m are the values of the streamwise and vertical velocity at each time instant m. The Reynolds stresses, τ_{Re} are also estimated as,

$$\tau_{\text{Re}}(y) = -\rho \langle u'v' \rangle_{\text{t}}(y), \tag{30}$$

where

$$\langle u'v' \rangle_{\text{t}}(y) = \frac{1}{n} \sum_{m=1}^{n} \left[u_{\text{m}}(y) - \langle U \rangle_{\text{t}}(y) \right] \left[v_{\text{m}}(y) - \langle V \rangle_{\text{t}}(y) \right]. \tag{31}$$

These values for the runs A/B and C/D are recorded at two different positions in the vertical: one close to the bottom, $y^+ = 11$, and one at the middle of the current height, $y^+ = 400$. The results are shown in Fig. 6(a–e). In both cases the main group of fluctuation peaks can be observed during the time period $(t - t_{\text{probe}})/t^* = 0 - 5$. As mentioned in Section 4.1, the time scale $5t^*$ roughly corresponds to the head of the current. Thus, after $(t - t_{\text{probe}})/t^* = 5$ the flow enters in a quasi-steady phase that characterizes the body of the current (Kneller et al., 1997). This can be confirmed by the quasi constant values of mean velocities and the important decrease of the Reynolds stresses. These results indicate that, the head of the current is strongly turbulent and is the region where the stronger mixing between the current and the ambient fluid occurs.

As shown in Fig. 6, the propagation of high Gr gravity currents is characterized by intense turbulent fluctuations. The different zones of intense turbulence and vorticity in gravity current flows have been studied and presented in Cantero et al. (2008). The area of interest in the present work is the region close to the bottom surface behind the front of the current. Fig. 7 shows a top-view of the structures formed in the turbulent layer close to the bottom boundary of the channel. For the eduction of the turbulent structures, the λ_2 criterion of Jeong and Hussain (1995) is used. This method identifies vortex cores as regions where high vorticity and pressure minima are present. The main features of this region are quasi-streamwise vortices and hairpin vortices inclined in the flow direction (Cantero et al., 2008), which are mainly concentrated to the region behind the front of the current ($x/H > 23$). As in channel flows, the turbulent structures in the vicinity of the wall are strongly interacting with the bed material. This interaction is further investigated in the next section.

In the present study, where a wall resolving LES is performed ($\Delta y^+ = 1$) the bed shear stress is obtained by $\tau_{\text{w}} = \mu(\text{d}u_1/y_1)$ where 1 corresponds to the first grid point off the wall. However, for the studies of sediment transport problems we are mainly interested on identifying the regions where the bed shear stress exceeds the critical value and the particles start to move. This quantity is called excess bed shear stress ($(\tau - \tau_{\text{cr}})/\tau_{\text{cr}}$) and its distribution is presented in Fig 8(a). In this figure, the white solid line indicates the position of the front. The excess bed shear stress is not homogeneously distributed: the peak values mainly appear just after the front of the current and below the billows. These peaks create elongated streaks of high positive and negative values (see Fig 8(a)). The streaks correlate with the lobes and clefs instabilities at the nose of the current, as also observed by Ooi et al. (2009). In Fig 8(b_1 and b_2) the time evolution of the excess bed shear stress at two different positions in the spanwise direction is presented. Position z_1 corresponds to the middle of the channel, whereas position z_2 corresponds to a point located a quarter of the width away from the right lateral wall (see Fig. 8(a)).

5. Interaction between current and sediment

In the present section, the erosion induced by the passage of the current above the mobile section of the bed is studied. Additionally, the effect of the entrained material on the dynamics of the current and the key mechanisms that influence the entrainment are investigated. Results for different Gr numbers and different grain sizes are illustrated. The deposition of the entrained ma-

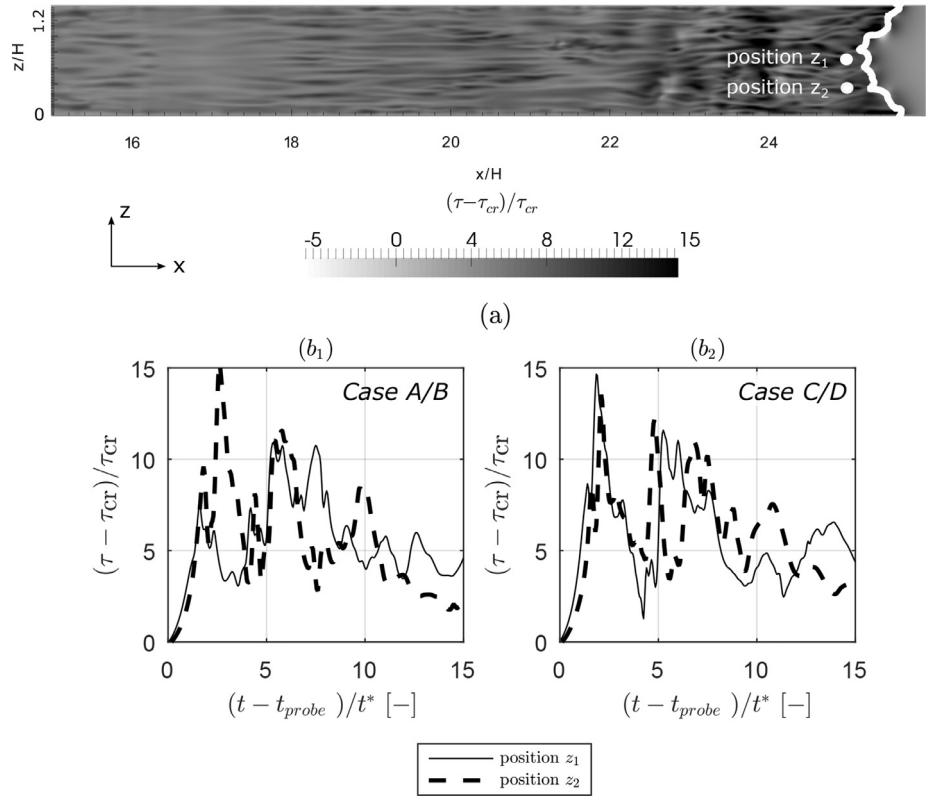

Fig. 8. (a) Top view of the instantaneous excess bed shear stress distribution at the bottom of the channel at time $t = 20$ s for case *B*. The white line in figure (a) represents the position of the front of the current. (b) Time evolution of the excess bed shear stress for case *A*/*B* and *C*/*D* (b_1 and b_2 respectively) at two different points in the spanwise direction. Middle point (solid line, z_2) and a point located at a quarter of the width away from the right lateral wall (dashed line, z_1).

terial and the formation of bed forms downstream of the mobile bed are not investigated in this paper.

5.1. Space and time distribution of the entrained sediment

The entrainment of bed material into suspension requires two simultaneous events. First the bed needs to be sheared and secondly the presence of turbulent motion is necessary to counteract the settling velocity of the entrained sediment, and to transport it up in the outer region of the flow. According to the results of the previous section, the front of the current is the region where these two requirements are fulfilled. Specifically, it has been shown that the region just after the front of the current is strongly turbulent with high peaks of vertical velocity, Reynolds shear stresses, and bed shear stress. Hence, this part of the flow shows a high pick-up sediment rate, whereas the body of the current is less powerful and settling is expected to dominate there.

However, due to the streaky distribution of the bed shear stress and of the instantaneous velocities in the spanwise direction, single point measurements are not sufficient. A wider picture of these two mechanisms over the whole channel is necessary. In Fig. 9 the streamwise distribution of the spanwise-averaged (a) excess bed shear stress, (b) vertical velocity, (c) vertical velocity fluctuations, and (d) Reynolds shear stresses are presented, for case *C*. The vertical black line plotted in Fig. 9 indicates the position of the front and the spanwise-averaged quantities are indicated by the symbol ($\langle\,\rangle$). The other cases have a behavior that is qualitatively similar, and are not shown here. The excess bed shear stress takes values higher than 1 (which means that the sediments start to move) in an area that corresponds roughly to half the length of the current. On the other hand, the vertical velocities and Reynolds shear stresses peaks are concentrated only in the head region. Thus, combining both results, the presence of the entrained sediment in the outer region of the flow is expected only in the head of the current. In the part of the current body where the excess bed shear stress is higher than 1, the bed material is expected to move within the small shear layer in the vicinity of the wall.

Snapshots of suspended sediment concentration resulting from the numerical simulations are shown only over a small window above the mobile reach focusing on the erosion ability of the current. The purpose of such visualization is to compare with images of entrained sediment recorded during the experiments by Zordan et al. (2017), which are taken from the side view. The numerical information complements and provides a quantification of what is obtained in the experiments, since these do not supply exact concentration measurements of the entrained bed material. The sediment concentration obtained from the simulations is processed in order to obtain a spanwise-average sediment concentration $\langle C\rangle(x, y)$ above the mobile bed. This corresponds to what an observer would perceive by looking at the current propagation above the mobile bed from the side. The beginning of the interrogation window is located at distance 2.7 m from the lock and its dimensions are $L_w = 0.24$ m $\times H_w = 0.2$ m $\times W_w = 0.75$ m in streamwise, vertical, and spanwise direction, respectively. The numerical results are collected every $(t - t_{probe})/t^* = 0.045$.

The sediment presence in the images can only be inferred by an analysis of the recorded shades. The salinity current corresponds to an area with high luminescence whereas the sediment forms darker areas. Thus, analyzing the brightness of each picture, it is possible to reconstruct the areas with high sediment concentration. The use of a salinity gradient for generating the current is here beneficial, because in this way the bed material remains

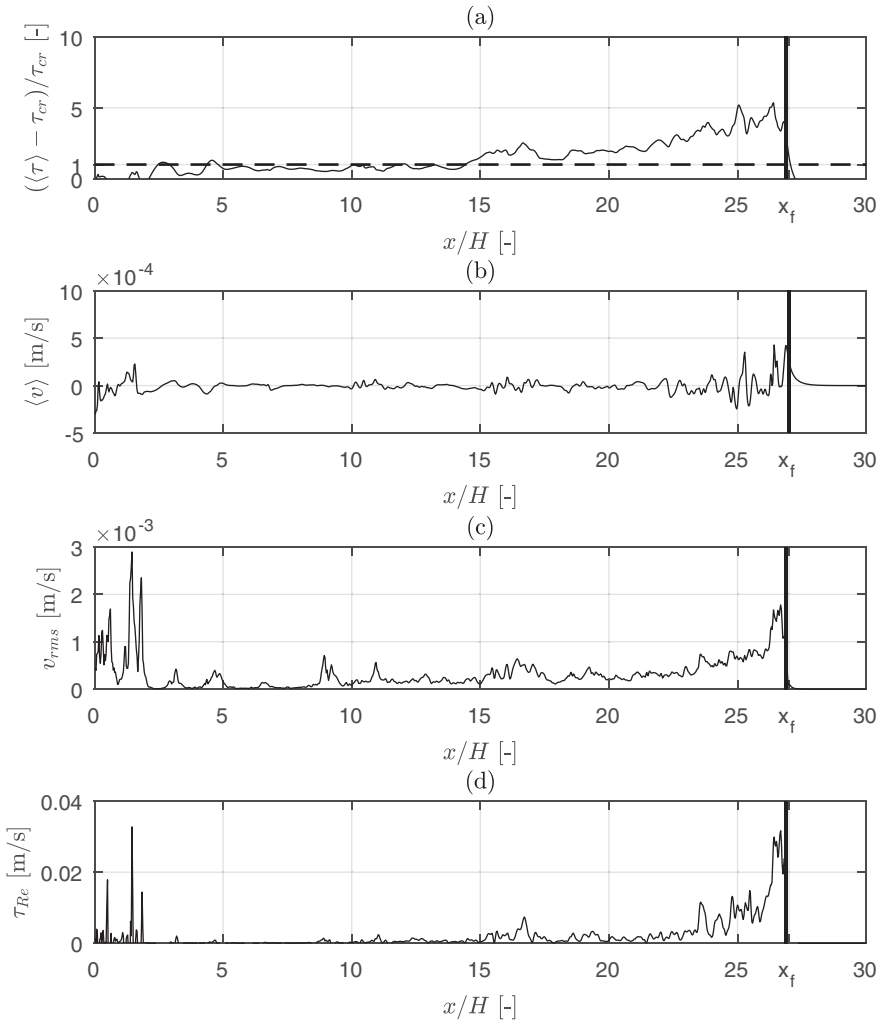

Fig. 9. Instantaneous plots for case *C*, at time instant $t_3 = (t - t_{\text{probe}})/t^* = 1.4$, of (a) spanwise averaged bed shear stress, (b) spanwise-averaged vertical velocity at height $y^+ = 11$, (c) vrms at height $y^+ = 11$ and (d) Reynolds shear stresses at height $y^+ = 11$. The vertical black line indicates the position of the front x_f.

clearly visible. Therefore, it is possible to detect it also inside the current. It is noteworthy that the precision, in the identification of the sharp images, is in the order of the pixel resolution, i.e., 0.5 mm/pixel as mentioned in Section 4.2. This experimental approach can provide a good qualitative estimation of the main features of the entrained sediment concentration. However, its main disadvantage is that an adequate way to relate these qualitative results with the quantitative data provided by the numerical simulations should be found. For this to be possible, a relationship that could connect the image luminescence to the concentration should exist. Unfortunately, this is not the case. Under these circumstances, the comparison between the experimental and numerical results should be intended in a qualitative sense.

Fig. 10 depicts the position of the current above the mobile bed along with the contour plots of the spanwise-averaged concentration obtained numerically, at 3 different time instants ($t_1 = (t - t_{\text{probe}})/t^* = 1$, $t_2 = 1.2$, and $t_3 = 1.4$). Moreover, the outlines of the areas (current and sediments), obtained in the laboratory with the procedure mentioned above, are denoted by the gray diamonds and crosses, respectively lines. The iso contour $C_{\text{th}} = 2.5 \times 10^{-6}$ of the numerical data, has been highlighted by a black dashed line to ease the comparison, since no concentration measurements are provided from the experiments. This value of concentration has been used also for the analysis presented in Fig. 11 presented below. The results show that sediment pick-up is mainly present in the head, which is in accordance with what has been argued in Fig. 9. In the vicinity of the wall the sediment concentration is higher due do the high shear. However, the suspended material diffuses over the whole height of the current due to the advection mechanisms acting in the head area. Moreover, the distribution of the suspended material has a shape similar to that of the head recirculation. Regarding the results coming from the pictures taken during the experiments, it is difficult to identify the movement of the sediment at the upper boundary of the current. This region is characterized by high mixing between the current and the ambient fluid which is also characterized by low luminescence in the pictures of the experimental results. This can explain the discrepancy between numerical and experimental result. Nevertheless, the upward movement behind the front is also visible in the experiments to some extent.

A quantitative estimation of the total area covered by sediment requires the determination of a threshold average concentration C_{th}, marking the boundary above which sediments are visible in the pictures. Identifying experimentally the exact value of the concentration threshold, C_{th}, is troublesome, thus requiring numerical calibration. In this case, a value of $C_{\text{th}} = 2.5 \times 10^{-6}$, is chosen in order to have an agreement with the physical evidence of the experiments. An equal treatment is necessary for the salinity threshold corresponding to the visible boundaries of the current, in this case chosen to be equal to $Sal_{\text{th}} = 0.02$ as proposed by

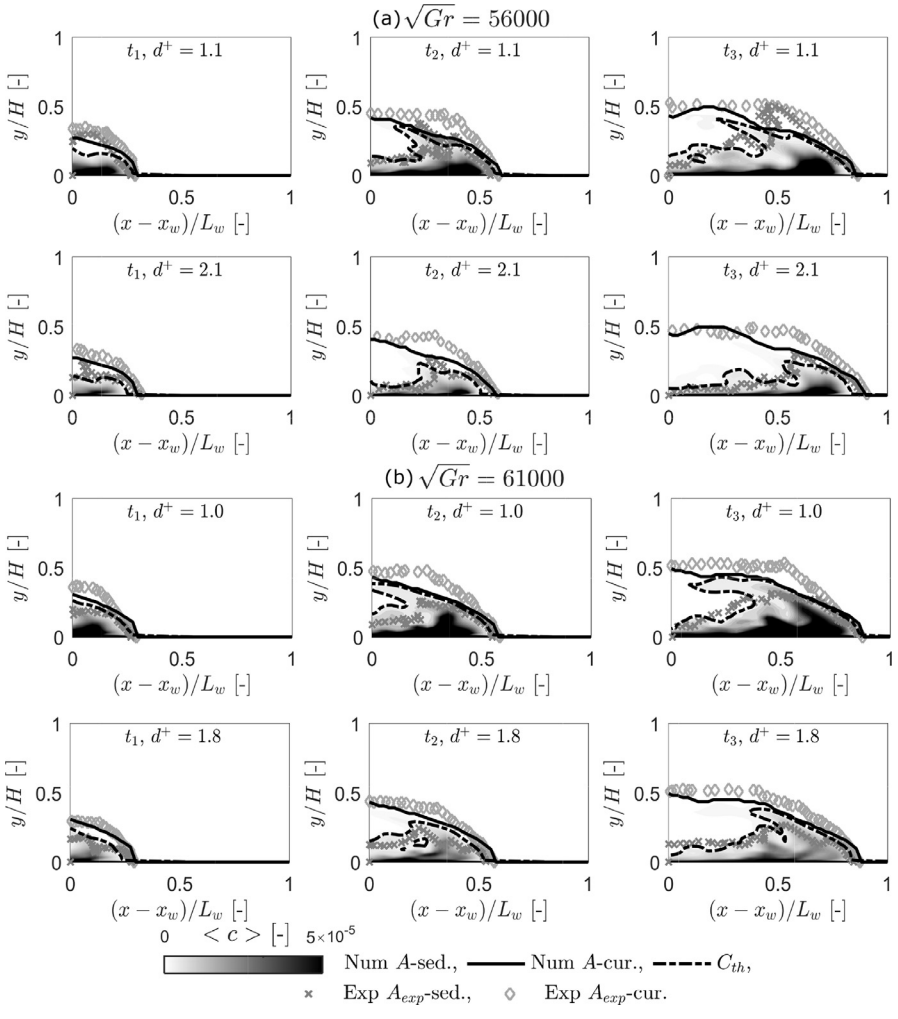

Fig. 10. Numerical and experimental sediment concentration and current shape at different time instants. The black solid lines shows the shape of the current, and the contour plots illustrate the spanwise-averaged sediment concentration, both calculated numerically. The experimental shape of the current and area covered by sediment are shown with gray diamonds and crosses, respectively. The dashed black line corresponds to the limit values $C_{\text{th}} = 2.5 \times 10^{-6}$. Each line of figures correspond to the cases *A, B, C*, and *D*, respectively.

Ottolenghi et al. (2016a). Once the threshold values are identified, a time history of the data collected in the interrogation window can be produced. The evolution of the total areas covered by sediment, A_{sed}, and the area covered by current, A_{sal} is thus tracked with the following procedure. The cells on the *xy* plane that contain a spanwise-average sediment concentration higher than the threshold parameter mentioned above are identified. The total area covered by these cells is calculated to obtain the area covered by sediments as function of time. The same procedure is also used to calculate the area that contains the gravity current.

$$A_{\text{sed}}(t) = \sum_{i}^{M} \Delta x_i \Delta y_i \zeta_i(t), A_{\text{sal}}(t) = \sum_{i}^{M} \Delta x_i \Delta y_i \xi_i(t), \tag{32}$$

where M corresponds to the number of the cells, and Δx_i and Δy_i are the size of each cell in the streamwise and vertical direction, respectively. Moreover,

$$\zeta_i(t) = \begin{cases} 1 & \text{if } \langle C_{\text{sed,i}}(t) \rangle \geq C_{\text{th}} \\ 0 & \text{otherwise,} \end{cases} \xi_i(t) = \begin{cases} 1 & \text{if } \langle C_{\text{sal,i}}(t) \rangle \geq Sal_{\text{th}} \\ 0 & \text{otherwise.} \end{cases} \tag{33}$$

Fig. 11 shows the time evolution of the total areas covered by the current and the sediment. The areas are made dimensionless using the area of the interrogation window. When the current arrives at the interrogation window the salinity area starts to increase. Moreover, at the same time the current reaches the mobile bed therefore the sediment areas start also to increase due to the erosion induced by the current. The time that is necessary for the front to cross the interrogation window corresponds to $(t - t_{\text{probe}})/t^* \sim 5$ (estimated taking into account the u_{front} and the length of the window). During this time period, the area covered by the current in Fig. 11 is increased. Then, the area remains constant, at a slightly lower value that corresponds to the body of the current where a constant mixing layer is formed. The area covered by the sediment starts to increase a bit after the moment in which the current enters the window and exhibits its peak when the front is still inside the interrogations window. After the head has passed, the area covered by sediment decreases until dropping to zero, since the sediment is advected downstream by the current and therefore dragged out from the interrogation window. These results are in agreement with the experimental data.

5.2. Influence of suspended sediment on the hydrodynamics of the current

As mentioned in Section 4.2, the front velocity of the current, for the cases studied here, is not altered when the current prop-

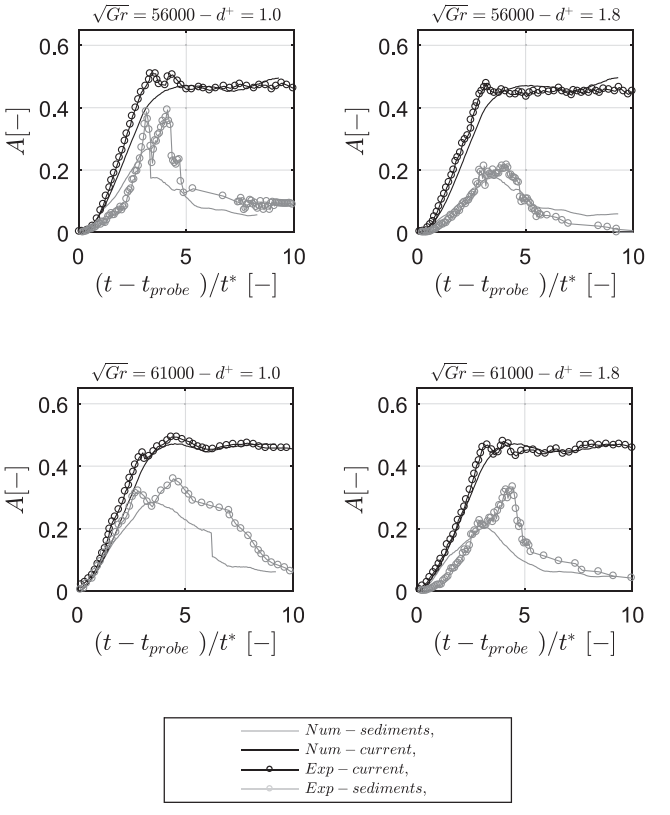

Fig. 11. Time evolution of the cumulative areas covered by the gravity current (black) and the sediment (gray) for cases *A, B, C*, and *D*. The numerical results are compared with experimental data: black circles for the gravity current and gray circles for the sediment are used.

agates over the mobile reach of the bed (see Fig. 4). This indicates that the concentration of the entrained particles is not strong enough to influence the dynamics of the current. To further investigate this aspect, the gradient Richardson number, Ri_g, for salinity and sediment concentration is back-calculated. The definition of the gradient Richardson number is the following:

$$\mathrm{Ri}_g = \frac{-\frac{g}{\rho_w}\frac{\partial\langle\rho\rangle}{\partial y}}{\left(\frac{\partial\langle u\rangle}{\partial y}\right)^2}, \tag{34}$$

where $\langle\rho\rangle$ denotes the spanwise-averaged density. The effect of salinity concentration on the density distribution can be calculated using the Eq. (4) and the effect of sediment concentration on the density distribution is expressed as:

$$\rho = \rho_w + (\rho_s - \rho_w)C_{sed} \tag{35}$$

However, the suspended sediment concentration is not homogeneously distributed inside the body of the current (the entrainment is higher in the head of the current compared to the body). Thus, a layer Richardson number (see Xu et al., 2006) at different cross sections in the streamwise direction is calculated as:

$$\mathrm{Ri}_{gx} = \frac{-\frac{g}{\rho_w}\frac{\partial\langle\rho_k\rangle}{\partial y}}{\left(\frac{\partial\langle u_k\rangle}{\partial y}\right)^2}, \tag{36}$$

where k denotes each cross section in the streamwise direction.

The Richardson number expresses the ratio of buoyancy forces to shear forces in the flow. This non-dimensional number has been widely used in literature to asses the stability of stratified shear flows. Increasing values of Ri_g indicate more and more stable stratification. Fig. 12 shows the calculated Ri_{gx} numbers based on salinity (column one), sediment (column two) and, both salinity and sediment (column three), for cases *A, B, C* and *D* at different streamwise positions above the mobile reach of the bed, at the time instant t_3, mentioned above. According to Armenio and Sarkar (2002), the Richardson number divides the flow in two main regimes: (i) the buoyancy-affected regime where $\mathrm{Ri}_{gx} < 0.25$ and (ii) the buoyancy-dominated regime where $\mathrm{Ri}_{gx} > 0.25$. The estimates of salinity-based gradient Richardson numbers show an extended area with $\mathrm{Ri}_{gx} > 0.25$, located in the mixing layer between the current and the ambient fluid. In this region stable stratification effects are present. The negative values of salinity Ri_{gx}, in the vicinity of the wall, correspond to unstable density gradients with active convective overturning. On the other hand, the calculated Ri_{gx} number for the suspended sediment gets values higher than 0.25 only locally, and mainly in case *A*. The total Ri_{gx} plotted at the last column of Fig. 12 does not show any substantial difference with regard to the salinity Ri_{gx}, plotted in the first column. This result suggests that stratification effects due to the suspended sediment is too small to have a dominant effect on the stability of the current front and confirms the assumption made in Section 4.2. Although, the suspended sediment may contribute to the reduction of the convection noticed at the lower part of the current.

The influence of the stable stratification, observed at the upper boundary of the current, on the suspended sediment distribution is also important. More clearly, the higher the values of the Richardson number, due to salinity, the lower turbulent mixing becomes. Thus, the increased stability inhibits the transfer of the suspended sediment across the boundary with the ambient fluid. In Fig. 10 the upper boundary of salinity, shown as gray solid line, demarks a limit on the distribution of sediments.

5.3. Mechanisms that influence entrainment

As mentioned before, for the entrainment of a grain into suspension two mechanisms are necessary: (a) a shear force which causes the motion of the grain, (b) an upward turbulent motion able to move the grain away of the bed and keep the sediment into suspension. In this section we investigate the importance of each of these mechanisms on the bed material entrainment induced by gravity currents.

In wall bounded flows the excess bed shear stress is the mechanism that forces the particles to move and leads to the initiation of erosion. Fig. 13(a) displays the top view of the excess bed shear stress distribution on the immediate vicinity of the bottom of the channel for case *A*. In Fig. 13(b) the suspended sediment concentration at the same plane is also shown. The suspended sediment concentration follows the streaky patterns of the bed shear stress, mentioned in Section 4 with higher values immediately after the front. The results for all the other cases follow the same patter. It is obvious that the dominant process at this stage is erosion and the settling velocity of the particles seems not to play a significant role.

As the particles start to move they interact with the vortical structures present inside the wall shear layer. This turbulence-particle interaction lifts the bed material up and moves it towards to the outer region of the flow (Niño and Garcia, 1996). Fig. 14 illustrates the suspended sediment concentration (isocontour equal to 0.0005 for case *A*). The pattern created by the sediment concentration surface can be compared with the dominant structures observed in Fig. 7. More specifically, at the nose of the current the sediment follow the hairpin vortices forming in this region, whereas farther upstream they correlate with the quasi-streamwise vortices. Moving toward the body of the current, the turbulent structures lose their coherence and the sediment entrainment decreases. The streaky patterns created by the

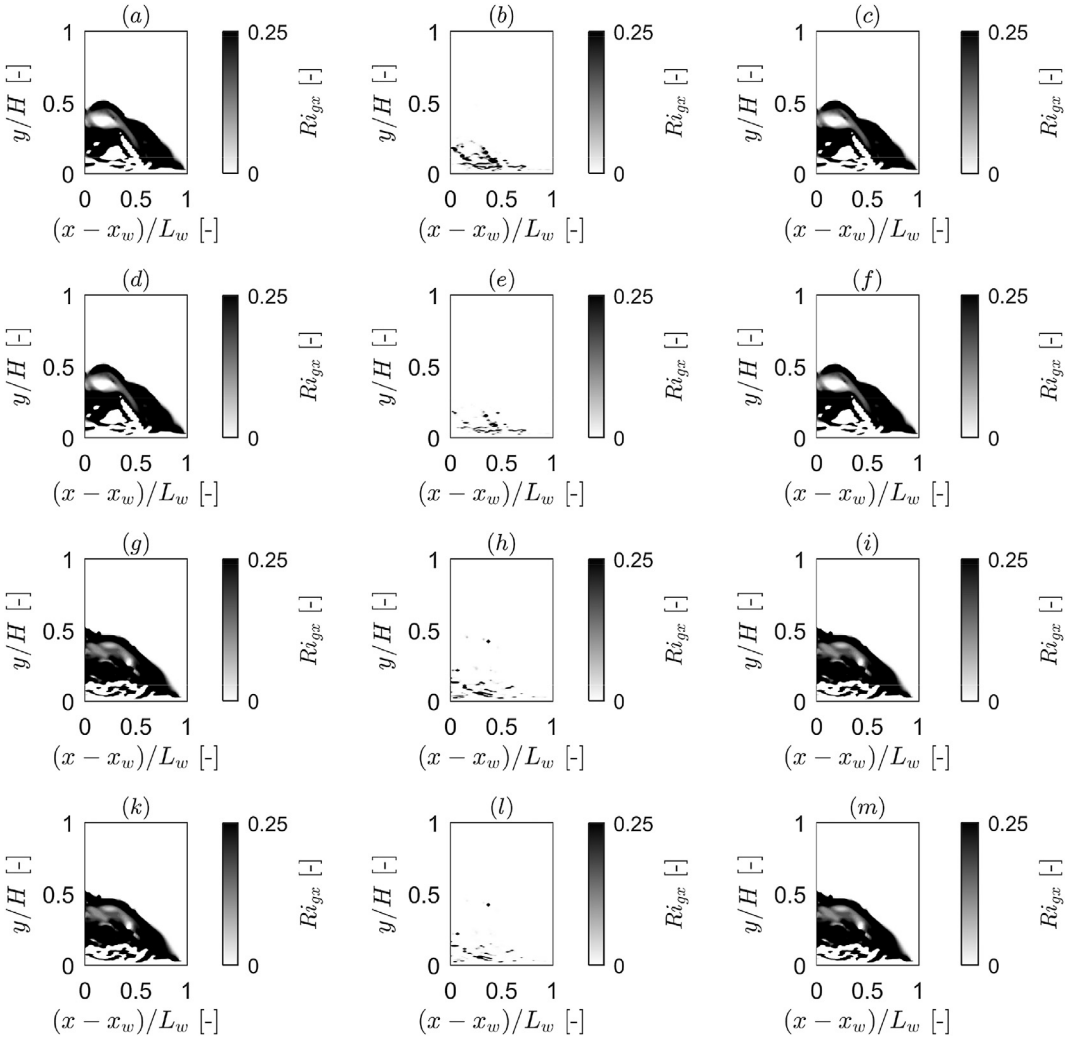

Fig. 12. Gradient Richardson number at different streamwise positions, at the time instant t_3 mentioned in Section 3.1. The first column correspond to the gradient Richardson number Ri_{gx} based on salinity, for cases *A, B, C,* and *D*, respectively. The second column corresponds to the Ri_{gx} based on the suspended sediment, for the same cases. The third column corresponds to the Ri_{gx} based on both salinity and suspended sediment.

sediment concentration isosurface extend for $\Delta x/H = 2$ upstream of the nose, in accordance with the streaky structures observed in Fig. 7(a).

The upward flow movements and the turbulent fluctuations have an influence on the suspension of the entrained material. In order to quantify this effect, three time-signals of relevant quantities are available from the data shown in Fig. 6. These are the Reynolds shear stresses τ_{Re}, the vertical velocity v, and the vertical velocity fluctuations v_{vrms}. To obtain a unique signal of such quantities over the vertical, a depth average has been computed over the height of the current. The peak values at the upper and bottom boundary of the current are smoothed out by this procedure. To estimate the contribution of these quantities, the cross correlation $R_{A_{\mathrm{sed}}\phi}(lag)$ of each signal with the time evolution of the total area covered by the sediment, A_{sed}, is calculated as,

$$R_{A_{\mathrm{sed}}\phi} = \begin{cases} \sum_{n=0}^{N-m-1} (A_{\mathrm{sed}})_{n+m}\phi_n, & \text{if } m \geq 0 \\ R_{A_{\mathrm{sed}}\phi}(-m), & \text{if } m < 0. \end{cases} \tag{37}$$

where N indicates the total time steps, m the time lag and ϕ corresponds to the signal that is correlated with the sediments. These correlations are normalized so that the autocorrelations of a signal at zero lag is equal to 1, obtaining R_{norm}. Such normalization allows the correlation coefficient to vary between 1 and -1 irrespectively of the numerical values of the signals.

The correlations relate A_{sed}, an integral quantity over the whole interrogation window with signals taken at the probe, placed before the window itself. Investigating various signals in different streamwise positions, it is concluded that every x-position inside the window is expected to register an equivalent signal. This is an important key for the interpretation of the results, which are presented in Fig. 15. The correlations reveal that the sediment entrainment is related to v_{vrms}, τ_{Re}, and v with a small time lag of about $t_{\mathrm{lag}}/t^* = 2$. This time corresponds to the moment when the first billow of the current start to break, and therefore the first group of large peaks of the kinematic quantities has completely entered the interrogation window. This is the time instant at which the sediment experiences the quickest diffusion upwards. However, the strong, initially upward velocities are followed by equally strong negative movements. This explains the negative correlation coefficients for positive time lags, which indicates that sediment continues to increase, inside the interrogation window, even if there is a drop on the vertical flow components and in turbulent fluctuations. This is because the head in this time frame is still inside the window, and the strong positive vertical components part of the head recirculation are still active.

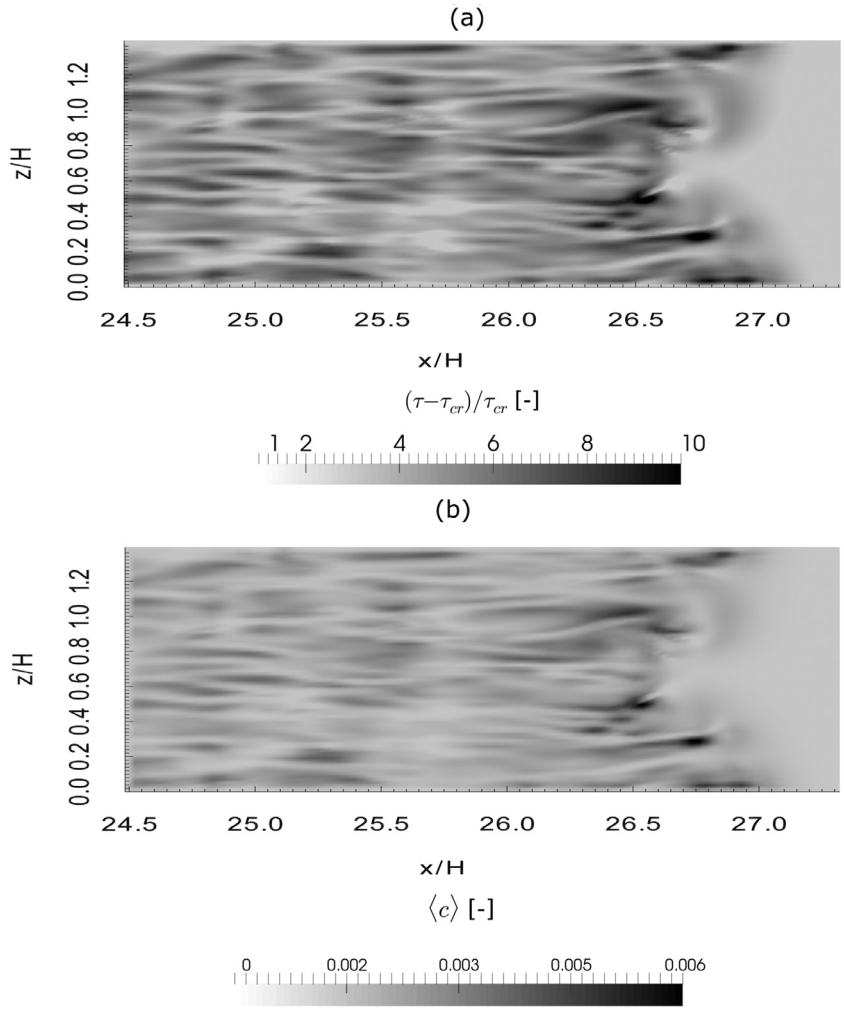

Fig. 13. (Top view of (a) the excess bed shear stress and (b) the suspended sediment concentration above the mobile bed for case *A* (at the time instant t_3 mentioned in Section 5.1).

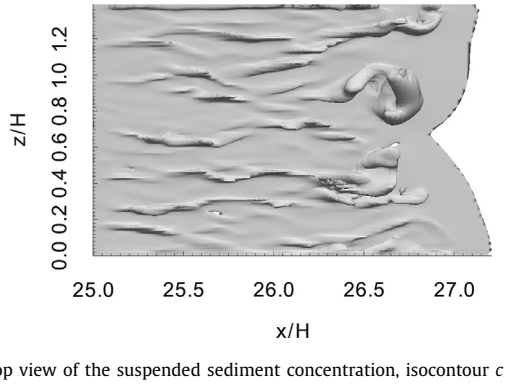

Fig. 14. Top view of the suspended sediment concentration, isocontour $c = 0.0005$, for case *A*. Only the region above the mobile bed is displayed, at the time instant t_3 mentioned in Section 5.1.

6. Conclusions

In the present paper the results of three-dimensional LES for salinity currents flowing over a mobile reach are presented and discussed. Four cases are investigated varying the Grashof number and the grain size of the erodible bed. The goal is to study the bed material entrainment and its interaction with the dynamics of the current. More specifically, the features of the flow dynamics that trigger bed material entrainment are identified and studied qualitatively and quantitatively. Additionally, the feedback of the entrained material on the gravity current is studied. The results give the possibility to understand in depth the interaction between the gravity current and the bed material and to indicate the mechanisms that play a role on the pick-up and suspension of sediment.

The main features of the flow are presented and compared with experimental results showing a good agreement. The analysis of the velocity field showed that the head of the current is strongly turbulent. In this region, the flow is characterized by intense streamwise and vertical velocity fluctuations, and by high peaks of bed shear stress. As a result, when the current passes over the erodible section of the bed, the region just behind the front of the current presents a high pick-up sediment rate. The entrained material is advected downstream by the head of the current and eventually settles further away. Additional flow features that play an important role on the lift-up of the bed material are the turbulent structures that form in the shear layer close to the wall immediately after the front of the current.

Details of the distribution of the suspended sediment concentration are presented at different time instants above the mobile section of the bed. The time evolution of the cumulative areas of the flow covered by the sediment is also calculated. These results indicate that the sediment starts to be entrained just after the front has entered the mobile reach and it achieves its peak some seconds after, when the head is still inside the interrogation win-

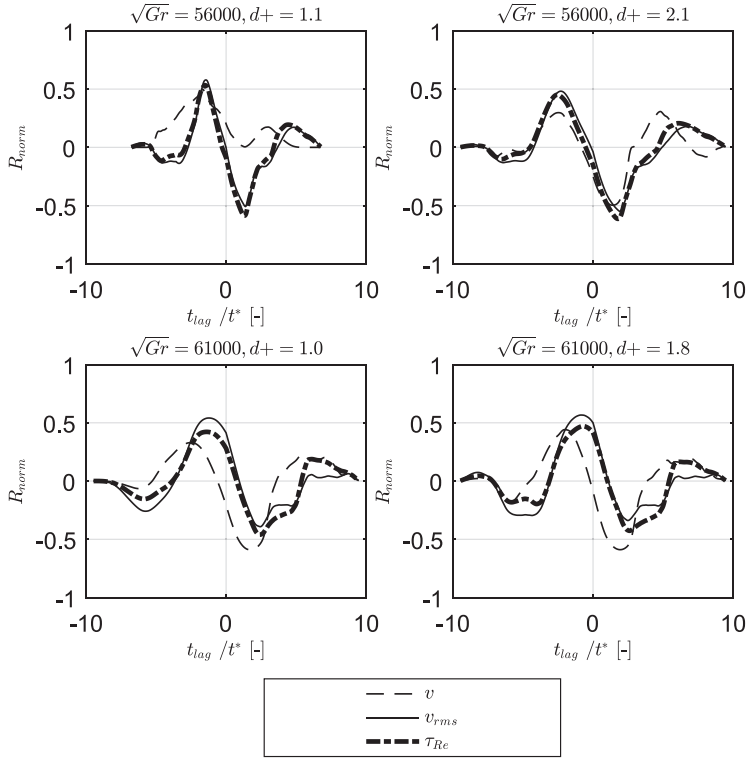

Fig. 15. Cross-correlations between the time signals of the hydrodynamic variables, v, v_{rms} and τ_{Re}, and the time evolution of the cumulative area covered by sediment for cases *A*, *B*, *C*, and *D*, respectively.

dow. The sediment is then advected downstream by the current head. In the body of the current, the area covered by suspended sediment drops to zero.

Furthermore, the current-sediment interaction is studied. The front velocity of the current does not show any significant change when the current flows above the mobile bed. To compliment this result, the gradient Richardson number, for salinity and suspended sediment concentration, at different streamwise positions is calculated. The plots of the gradient Richardson number reveal strong stratification effects due to salinity, especially at the mixing interface. However, for the cases studied here, the stratification due to suspended sediments was too small to have an important influence on the stability conditions of the current. Furthermore, it is concluded that, the stable salinity gradients present on the mixing interface, inhibits the transfer of the suspended particles into the ambient fluid. Thus, although the suspended sediment is distributed over the whole height of the current, it remains confined in it.

The suspended sediment concentration on the bottom of the channel follows the distribution of the excess bed shear stress, showing that erosion is the dominant process and that deposition does not play an important role in this region. After the sediment has started moving due to the shear stress, it is transported in the outer region of the flow following the turbulent structures formed in the shear layer close to the wall. To quantify the importance of the upward flow and of the turbulent fluctuations on the overall suspended bed material, the time signals of the Reynolds shear stresses τ_{Re}, of the vertical velocity v, and of the vertical velocity fluctuations v_{vrms} are correlated with the time evolution of the areas covered by the sediment. The analysis shows that the pick-up and the transport of the entrained bed material is due to the excess stress and the turbulence that appear in the front region of the current. Specifically, after the incipient motion of the sediment and their lift-up from the bed, the vertical velocity of the flow and the upward turbulent motion are able to counteract the falling velocity of the particles and maintain the sediment into suspension.

The results regarding the suspended sediment are studied in a small interrogation window. Under these conditions the settling velocity seems to be of minor importance since the time scale given by settling is quite larger than the flow time scale. However, the sediments are still expected to deposit beyond the end of the mobile reach, forming bed forms that could follow an analogous pattern to that observed for the bed shear stress. Future work will be devoted to an in-depth study of this second part of the transport process. The influence of the bed deformation due to erosion on the current propagation in the studied conditions is negligible. However, for more erosive currents (e.g., for higher values of the Grashof number or different characteristics of the bed material), this is expected to back-influence the dynamics of the current. For a study of this two-way coupling between sediment and current a numerical tool able to process moving boundaries would be necessary. Simulating cases with higher erosion could also help identifying the threshold point at which the suspended sediment concentration starts to influence the buoyancy of the current, an aspect which requires further studies.

Acknowledgements

The research leading to these results received funding from the People Programme (Marie Curie Actions) of the European Union's Seventh Framework Programme FP7/2007-2013/ under REA grant agreement no 607394-SEDITRANS. This paper reflects only the authorsâ view and the Commission and REA are not responsible for any use that may be made of the information it contains. The author F.K. is grateful to S. López Castaño for fruitful discussions and for providing some post-processing routines and advises. The ex-

perimental data can be made available, upon request, by J. Zordan and C. Juez.

References

Akiyama, B.J., Stefan, H., 1986. Turbidity current with erosion and deposition. J. Hydraul. Eng. I (12), 1473–1496.

Armenio, V., Sarkar, S., 2002. An investigation of stably stratified turbulent channel flow using large-eddy simulation. J. Fluid Mech. 459 (May), 1–42. https://doi.org/10.1017/S0022112002007851.

Baas, J.H., McCaffrey, W.D., Haughton, P.D.W., Choux, C., 2005. Coupling between suspended sediment distribution and turbulence structure in a laboratory turbidity current. J. Geophys. Res. 110 (11), 1–20. https://doi.org/10.1029/2004JC002668.

Benjamin, T.B., 1967. Gravity currents and related phenomena. J. Fluid Mech. 31 (2), 209–248. https://doi.org/10.1017/S0022112068000133.

Cantero, M.I., Balachandar, S., García, M.H., Bock, D., 2008. Turbulent structures in planar gravity currents and their influence on the flow dynamics. J. Geophys. Res. 113 (8), 1–22. https://doi.org/10.1029/2007JC004645.

Constantinescu, G., 2014. LES of lock-exchange compositional gravity currents: a brief review of some recent results. Environ. Fluid Mech. 14 (2), 295–317. https://doi.org/10.1007/s10652-013-9289-0.

Cossu, R., Wells, M.G., 2012. A comparison of the shear stress distribution in the bottom boundary layer of experimental density and turbidity currents. Eur. J. Mech., B/Fluids 32 (1), 70–79. https://doi.org/10.1016/j.euromechflu.2011.09.006.

Dallali, M., Armenio, V., 2015. Large eddy simulation of two-way coupling sediment transport. Adv. Water Resour. 81 (December), 33–44. https://doi.org/10.1016/j.advwatres.2014.12.004.

Eames, I., Hogg, A.J., Gething, S., Dalziel, S.B., 2001. Resuspension by saline and particle-driven gravity currents. J. Geophys. Res. 106 (7), 14–95. https://doi.org/10.1029/2000jc900146.

Fernandez Luque, R., Van Beek, R., 1976. Erosion and transport of bed-load sediment. J. Hydraul. Res. 14 (October 2014), 127–144. https://doi.org/10.1080/00221686709499677.

Fine, I.V., Rabinovich, A.B., Bornhold, B.D., Thomson, R.E., Kulikov, E.A., 2005. The grand banks landslide-generated tsunami of november 18, 1929: preliminary analysis and numerical modeling. Mar. Geol. 215 (1–2 SPEC. ISS.), 45–57. https://doi.org/10.1016/j.margeo.2004.11.007.

Franca, M.J., Lemmin, U., 2006. Eliminating velocity aliasing in acoustic Doppler velocity profiler data. Meas. Sci. Technol. 17 (2), 313–322. https://doi.org/10.1088/0957-0233/17/2/012.

Garcia, M., Parker, G., 1993. Experiments on the entrainment of sediment into suspension by a dense bottom current. J. Geophys. Res. 98, 4793. https://doi.org/10.1029/92JC02404.

Gonzalez-Juez, E., Meiburg, E., Tokyay, T., Constantinescu, G., 2010. Gravity current flow past a circular cylinder: forces, wall shear stresses and implications for scour, 649. https://doi.org/10.1017/S002211200999334X.

Hallworth, M.A., Huppert, H.E., Phillips, J.C., Sparks, R.S.J., 1996. Entrainment into two-dimensional and axisymmetric turbulent gravity currents. J. Fluid Mech. 308 (1996), 289–311. https://doi.org/10.1017/s0022112096001486.

Härtel, C., Carlsson, F., Thunblom, M., 2000a. Analysis and direct numerical simulation of the flow at a gravity-current head. Part 2. The lobe-and-cleft instability. J. Fluid Mech. 418, 213–229. https://doi.org/10.1017/S0022112000001270.

Härtel, C., Meiburg, E., Necker, F., 2000b. Analysis and direct numerical simulation of the flow at a gravity-current head. Part 1. Flow topology and front speed for slip and no-slip boundaries. J. Fluid Mech. 418, 189–212. https://doi.org/10.1017/S0022112000001221.

Huppert, H.E., Simpson, J.E., 1980. The slumping of gravity currents. J. Fluid Mech. 99 (04), 785. https://doi.org/10.1017/S0022112080000894.

IOC, SCOR, IAPSO, 2010. The international thermodynamic equation of seawater 2010: valculation and use of thermodynamic properties, 56.

Jeong, J., Hussain, F., 1995. On the identification of a vortex. J. Fluid Mech. 285, 69–94. https://doi.org/10.1017/S0022112095000462.

Kneller, B.C., Bennett, S.J., McCaffrey, W.D., 1997. Velocity and turbulence structure of density currents and internal solitary waves: potential sediment transport and the formation of wave ripples in deep water. Sediment. Geol. 112 (3–4), 235–250. https://doi.org/10.1016/S0037-0738(97)00031-6.

Kraft, S., Wang, Y., Oberlack, M., 2011. Large eddy simulation of sediment deformation in a turbulent flow by means of level-Set method. J. Hydraul. Eng. 137 (11), 1394–1405. doi: 10.1061/(ASCE)HY.1943-7900.0000439.

Lemmin, U., Rolland, T., 1997. Acoustic velocity profiler for laboratory and field studies. J. Hydraul. Eng. 123 (12), 1089–1098.

Leonard, B., 1979. A stable and accurate convective modelling procedure based on quadratic upstreaminterpolation. Comput. Methods Appl. Mech. Eng. 19, 59–98.

Leonardi, A., Cabrera, M., Wittel, F.K., Kaitna, R., Mendoza, M., Wu, W., Herrmann, H.J., 2015. Granular-front formation in free-surface flow of concentrated suspensions. Phys. Rev. E - Stat., Nonlinear, Soft Matter Phys. 92 (5), 1–13. https://doi.org/10.1103/PhysRevE.92.052204.

Lilly, D.K., 1992. A proposed modification of the Germano subgridscale closure method. Phys. Fluids A 4 (3), 633–635. https://doi.org/10.1063/1.858280.

Lombardi, V., Adduce, C., La Rocca, M., 2017. Unconfined lock-exchange gravity currents with variable lock width: laboratory experiments and shallow-water simulations. J. Hydraul. Res. 1–13.

Mattioli, M., Alsina, J.M., Mancinelli, A., Miozzi, M., Brocchini, M., 2012. Experimental investigation of the nearbed dynamics around a submarine pipeline laying on different types of seabed: the interaction between turbulent structures and particles. Adv. Water Resour. 48, 31–46. https://doi.org/10.1016/j.advwatres.2012.04.010.

Meneveau, C., Lund, T., Cabot, W., 1996. A Lagrangian dynamic subgrid-scale model of turbulence.

Necker, F., Härtel, C., Kleiser, L., Meiburg, E., 2002. High-resolution simulations of particle-driven gravity currents. Int. J. Multiphase Flow 28 (2), 279–300. https://doi.org/10.1016/S0301-9322(01)00065-9.

Necker, F., Härtel, C., Kleiser, L., Meiburg, E., 2005. Mixing and dissipation in particle-driven gravity currents. J. Fluid. Mech. 545 (-1), 339–372. https://doi.org/10.1017/S0022112005006932.

Niño, Y., Garcia, M.H., 1996. Experiments on particle-turbulence interactions in the near-wall region of an open channel flow: implications for sediment transport. J. Fluid Mech. 326, 285–319. https://doi.org/10.1017/S0022112096008324.

Nogueira, H.I., Adduce, C., Alves, E., Franca, M.J., 2014. Dynamics of the head of gravity currents. Environ. Fluid Mech. 14 (2), 519–540. https://doi.org/10.1007/s10652-013-9315-2.

Nogueira, H.I.S., Adduce, C., Alves, E., Franca, M.J., 2013. Analysis of lock-exchange gravity currents over smooth and rough beds. J. Hydraul. Res. 51 (4), 417–431. https://doi.org/10.1080/00221686.2013.798363.

Ooi, S.K., Constantinescu, G., Weber, L., 2009. Numerical simulations of lock-exchange compositional gravity current. J. Fluid Mech. 635 (2009), 361. https://doi.org/10.1017/S0022112009007599.

Ottolenghi, L., Adduce, C., Inghilesi, R., Roman, F., Armenio, V., 2016a. Mixing in lock-release gravity currents propagating up a slope. Phys. Fluids 28 (5). https://doi.org/10.1063/1.4948760.

Ottolenghi, L., Adduce, C., Inghilesi, R., Armenio, V., Roman, F., 2016b. Entrainment and mixing in unsteady gravity currents. J Hydraul. Res. 54 (5), 541–557.

Ottolenghi, L., Adduce, C., Roman, F., Armenio, V., 2017a. Analysis of the flow in gravity currents propagation up a slope. Ocean Modell. 115, 1–13.

Ottolenghi, L., Cenedese, C., Adduce, C., 2017b. Entrainment in a dense current flowing down a rough sloping bottom in a rotating fluid. J. Phys. Oceanogr. 47 (3), 485–498. https://doi.org/10.1175/JPO-D-16-0175.1.

Papanicolaou, A., Barkdoll, B., 2011. Sediment Dynamics upon Dam Removal. American Society of Civil Engineers.

Parker, G., Fukushima, Y., Pantin H., M., 1986. Self-accelerating turbidity currents. J. Fluid. Mech. 171, 145–181.

Parker, G., Garcia, M., Fukushima, Y., Yu, W., 1987. Experiments on turbidity currents over an erodible bed experiments on turbidity currents over an erodible bed. J. Hydraul. Res. 25 (February), 123–147. https://doi.org/10.1080/00221688709499292.

van Rijn, L.C., 1984. Pick-up functions.pdf. J. Hydraul. Eng. 110 (10), 1494–1502.

Roman, F., Stipcich, G., Armenio, V., Inghilesi, R., Corsini, S., 2010. Large eddy simulation of mixing in coastal areas. Int. J. Heat Fluid Flow 31 (3), 327–341. https://doi.org/10.1016/j.ijheatfluidflow.2010.02.006.

Rottman, J.W., Simpson, J.E., 1983. Gravity currents produced by instantaneous releases of a heavy fluid in a rectangular channel. J. Fluid Mech. 135, 95–110. https://doi.org/10.1017/S0022112083002979.

Schleiss, A.J., Franca, M.J., Juez, C., De Cesare, G., 2016. Reservoir sedimentation. J. Hydraul. Res. 54 (6), 595–614. https://doi.org/10.1080/00221686.2016.1225320.

Sequeiros, O.E., Spinewine, B., Beaubouef, R.T., Sun, T., Garcia, M.H., Parker, G., 2010a. Bedload transport and bed resistance associated with density and turbidity currents. Sedimentology 57 (6), 1463–1490. https://doi.org/10.1111/j.1365-3091.2010.01152.x.

Sequeiros, O.E., Spinewine, B., Beaubouef, R.T., Sun, T., García, M.H., Parker, G., 2010b. Characteristics of velocity and excess density profiles of saline underflows and turbidity currents flowing over a mobile bed. J. Hydraul. Eng. 136 (7), 412–433. https://doi.org/10.1061/(ASCE)HY.1943-7900.0000200.

Simpson, J.E., 1972. Effects of the lower boundary on the head of a gravity current. J Fluid Mech 53 (04), 759–768. https://doi.org/10.1017/S0022112072000461.

Simpson, J.E., 1982. Gravity currents in the laboratory, atmosphere, and ocean. Annu. Rev. Fluid Mech. 14 (Hoult 1972), 213–234. https://doi.org/10.1146/annurev.fl.14.010182.001241.

Simpson, J.E., 1997. Gravity Currents: In the Environment and the Laboratory. Cambridge university press.

Theiler, Q., Franca, M.J., 2016. Contained density currents with high volume of release. Int. Assoc. Sedimentol. Spec. Publ. 1820–1842. https://doi.org/10.1111/sed.12295.

Van Rijn, L.C., 1984. Sediment transport part I: bed load transport.. J. Hydraul. Eng. 110 (10), 1431–1456. https://doi.org/10.1061/(ASCE)0733-9429(1987)113:9(1187).

Vanoni, V.A., 1975. Sedimentation Engineering. ASCE Task Committee for the Preparation of the Manual on Sedimentation of the Sedimentation Committee of the Hydraulics Division Published.

Vinokur, M., 1983. On one-Dimensional stretching functions for finite difference calculations. J. Comput. Phys. 50 (2), 215–234. https://doi.org/10.1016/0021-9991(83)90065-7.

Xu, X., Chang, Y.S., Peters, H., Özgökmen, T.M., Chassignet, E.P., 2006. Parameterization of gravity current entrainment for ocean circulation models using a high-order 3D nonhydrostatic spectral element model. Ocean Modell. 14 (1–2), 19–44. https://doi.org/10.1016/j.ocemod.2006.02.006.

Zanke, U., 1977. Berechnung der sinkgeschwindigkeiten von sedimenten. Technical Report.

Zordan, J., Juez, C., Schleiss, A.J., Franca, M.J., 2017. Experimental results on sediment entrainment by gravity currents 6865 (1), 1453–1458.